



# Hyperactivity of the CD155 immune checkpoint suppresses anti-viral immunity in patients with coronary artery disease

Tuantuan V. Zhao<sup>1</sup>, Zhaolan Hu<sup>1</sup>, Shozo Ohtsuki<sup>1</sup>, Ke Jin<sup>1</sup>, Bowen Wu<sup>1</sup>, Gerald J. Berry<sup>2</sup>, Robert L. Frye<sup>1</sup>, Jörg J. Goronzy<sup>1,3</sup> and Cornelia M. Weyand<sup>1,3</sup>✉

**Pre-existent cardiovascular disease is a risk factor for weak anti-viral immunity, but underlying mechanisms remain undefined. Here we report that patients with coronary artery disease (CAD) have macrophages (M $\phi$ ) that actively suppress the induction of helper T cells reactive to two viral antigens: the severe acute respiratory syndrome coronavirus 2 (SARS-CoV-2) spike protein and the Epstein-Barr virus (EBV) glycoprotein 350. CAD M $\phi$  overexpressed the methyltransferase METTL3, promoting the accumulation of N<sup>6</sup>-methyladenosine (m<sup>6</sup>A) in poliovirus receptor (PVR) mRNA. m<sup>6</sup>A modifications of positions 1635 and 3103 in the 3' untranslated region of PVR mRNA stabilized the transcript and enhanced surface expression of PVR-encoded CD155. As a result, the patients' M $\phi$  abundantly expressed the immunoinhibitory ligand CD155 and delivered negative signals to CD4<sup>+</sup> T cells expressing CD96 and/or TIGIT receptors. Compromised antigen-presenting function of METTL3<sup>hi</sup>CD155<sup>hi</sup> M $\phi$  diminished anti-viral T cell responses in vitro and in vivo. Low-density lipoprotein and its oxidized form induced the immunosuppressive M $\phi$  phenotype. Undifferentiated CAD monocytes had hypermethylated PVR mRNA, implicating post-transcriptional RNA modifications in the bone marrow in shaping anti-viral immunity in CAD.**

Pre-existing cardiovascular diseases, such as hypertension, CAD, cardiac arrhythmias and congestive heart failure, are strong risk factors for severe viral disease, complicated by high morbidity and mortality rates<sup>1,2</sup>. In addition, individuals with cardiovascular comorbidities fail to respond adequately against vaccines<sup>3</sup>. Poor anti-viral immunity in patients with CAD has been exemplified during the recent SARS-CoV-2 pandemic, where a history of CAD was associated with severe symptoms<sup>4</sup>. Patients with CAD generate weak immune responses against varicella zoster virus<sup>4</sup>, and chronic EBV infection has been associated with cardiovascular disease<sup>5,6</sup>. Although the relationship between viral immunity and progression of atherosclerotic disease remains insufficiently understood, the recent pandemic has made clear that a better understanding of protective immunity is needed to inform therapeutic management of virally infected patients with pre-existent cardiovascular disease.

Protection against and clearance of viral pathogens depends on the induction of adaptive immunity—in particular, priming and expansion of CD4<sup>+</sup> T cells that help antibody-producing B cells and virus-specific CD8<sup>+</sup> killer T cells<sup>7</sup>. SARS-CoV-2-specific CD4<sup>+</sup> T cells are detected in the peripheral blood of all Coronavirus Disease 2019 (COVID-19) convalescent patients<sup>8</sup>. Patients who have recovered from COVID-19 infection carry CD4<sup>+</sup> T cells with specificity for the viral spike and nucleocapsid antigens<sup>9</sup>. A subset of individuals testing negative for SARS-CoV-2 possess such CD4<sup>+</sup> T cells, probably induced by the endemic human coronaviruses that cause upper and lower respiratory tract infections in children and adults. Similarly, CD4<sup>+</sup> T cells are critical in protecting the host against deleterious effects of EBV infection<sup>10</sup>.

Patients with CAD have abnormalities in their innate and adaptive immune system. Transcriptomic and cytometric single-cell

analysis of atherosclerotic plaque lesions has identified T cells and M $\phi$  as the dominant tissue-residing cell types (10% M $\phi$  and 65% T cells, most being CD4<sup>+</sup> T cells<sup>11</sup>). The precise contribution of CD4<sup>+</sup> T cells in inducing and sustaining atherosclerosis is not well-defined, but patients with CAD have expanded clonotypes of IFN- $\gamma$ <sup>high</sup>-producing CD4<sup>+</sup>CD28<sup>-</sup> T cells<sup>12</sup>. These CD4<sup>+</sup> T cells are cytotoxic toward endothelial cells, jeopardizing vascular integrity<sup>13</sup>. Besides their role as tissue-destructive effector cells and their contribution in lipid uptake, M $\phi$  serve as antigen-presenting cells, a pinnacle position in the induction of adaptive immunity. M $\phi$  from patients with CAD suppress anti-viral T cell immunity due to aberrant expression of the co-inhibitory ligand PD-L1 (ref. <sup>14</sup>). Whether this defect has relevance in COVID-19 infection and in persistent EBV infection is unknown.

Like other professional antigen-presenting cells, M $\phi$  express an array of co-stimulatory and co-inhibitory ligands that influence communication with interacting T cells. M $\phi$  critically regulate the balance of T cell activation, tolerance and immunopathology by delivering activating and suppressive signals, with PD-L1 and the poliovirus receptor (PVR, CD155) instructing T cells to abort their activation program. CD155, a transmembrane glycoprotein from the nectin-like family of proteins, is typically expressed on monocytes, M $\phi$  and myeloid dendritic cells<sup>15</sup> and binds to three receptors on the surface of T cells and natural killer cells to transmit a stop signal: TIGIT (T cell immunoreceptor with Ig and ITIM domains), CD96 and CD226 (ref. <sup>16</sup>). Tumor cells abundantly express CD155, promoting immune-evasive strategies and assigning a role for CD155 blockade in anti-tumor immunotherapy<sup>17</sup>.

The intensity of T cell activation ultimately depends on the stimulatory–inhibitory ligand balance on antigen-presenting cells, subject to transcriptional or post-transcriptional regulation.

<sup>1</sup>Department of Medicine, Mayo Clinic Alix School of Medicine, Rochester, MN, USA. <sup>2</sup>Department of Pathology, Stanford University School of Medicine, Stanford, CA, USA. <sup>3</sup>Department of Medicine, Stanford University School of Medicine, Stanford, CA, USA. ✉e-mail: [cweyand@stanford.edu](mailto:cweyand@stanford.edu)

mRNA modifications are recognized as major post-transcriptional processes determining gene expression<sup>18</sup>. As the most prevalent reversible modification on mRNA, m<sup>6</sup>A regulates transcript stability, alternative splicing and translation<sup>18,19</sup>. Controlled by a group of regulatory proteins subdivided into ‘writer’, ‘reader’ and ‘eraser’ proteins, m<sup>6</sup>A is relevant for multiple cell types<sup>20</sup>. m<sup>6</sup>A is generated when the METTL3/METTL14/WTAP complex adds a methyl group at position N<sup>6</sup> of adenosine<sup>21</sup>. In mice, METTL3 deficiency leads to embryonic lethality<sup>22</sup>. The METTL3-mediated m<sup>6</sup>A modification controls tumor proliferation and invasion<sup>23</sup>. In the cardiovascular system, METTL3 has relevance in cardiomyocyte remodeling and hypertrophy<sup>24</sup>. METTL3 promotes macrophage polarization toward the pro-inflammatory M1 subtype by methylation of *STAT1* mRNA<sup>25</sup> and supports dendritic cell maturation<sup>26</sup>.

Here we define molecular mechanisms underlying the deficit of patients with cardiovascular disease to generate protective anti-viral immunity. Patients with CAD failed to induce CD4<sup>+</sup> T cell responses against SARS-CoV-2 and EBV antigens, a condition *sine qua non* for effective and sterilizing host protection. COVID-19 vaccination could not repair the inability of patients with CAD in expanding anti-SARS-CoV-2-reactive T cells. The immune defect derived from inadequate viral antigen presentation by M $\phi$ , caused by inappropriate expression of the inhibitory ligand CD155 (encoded by *PVR*). CD155<sup>hi</sup> antigen-presenting cells dampened induction of adaptive immunity by ligating the inhibitory receptors TIGIT and CD96 on memory CD4<sup>+</sup> T cells. Excess CD155 expression was a function of prolonged mRNA stability, downstream of the highly active methyltransferase METTL3 and enrichment of m<sup>6</sup>A-modified *PVR* mRNA. Small interfering RNA (siRNA)-mediated suppression of *PVR* and *METTL3*, as well as CD155-blocking antibodies, rescued the responsiveness of CD4<sup>+</sup> T cells against viral antigens. METTL3<sup>hi</sup> expression occurred early in the life cycle of monocytes and macrophages. The data define antigen-presenting M $\phi$  as critical effectors in anti-viral immunity, mechanistically link host protection to RNA epigenetics and specify m<sup>6</sup>A editing as a rate-limiting step in the induction of protective immunity. Targeting m<sup>6</sup>A regulators to control the CD155 immune checkpoint holds promise for improved management of viral infection in high-risk individuals.

## Results

**Patients with CAD fail to generate anti-viral T cell responses.** We developed an *ex vivo* assay system to probe the ability of patients with CAD and healthy, age-matched controls to induce SARS-CoV-2-specific and EBV-specific T cells. Peripheral blood mononuclear cells (PBMCs) from patients and control individuals were pulsed with a mixture of the two major SARS-CoV-2 antigens: SARS-CoV-2 spike (S) and nucleocapsid (N) proteins. In parallel, PBMCs were stimulated with EBV glycoprotein gp350, the most abundant glycoprotein expressed on the EBV envelope and the major target for neutralizing antibodies. We assessed the robustness of anti-viral T cell responses by monitoring the accumulation of secreted IFN- $\gamma$  (Fig. 1a). SARS-CoV-2-induced IFN- $\gamma$  concentrations averaged at

98 pg ml<sup>-1</sup> in cultures from healthy individuals, but patients with CAD produced only 43 pg ml<sup>-1</sup> (Fig. 1b and Extended Data Fig. 1b). Also, antigen-reactive T cells defined by the co-expression of CD69 and CD40L<sup>27</sup> were quantified by flow cytometry (Extended Data Fig. 1a). On day 5 after antigen stimulation, 0.77% of healthy T cells had the CD3<sup>+</sup>CD69<sup>+</sup>CD40L<sup>+</sup> phenotype, whereas this population was only half the size in patients with CAD (Fig. 1c). Comparison of CD69<sup>+</sup>CD40L<sup>+</sup> frequencies within the CD4<sup>+</sup> and CD8<sup>+</sup> subpopulations assigned the blunted response of patients with CAD to the CD4<sup>+</sup> subset (Extended Data Fig. 1c). In freshly harvested cell populations, patients with CAD and healthy controls had a similar distribution of CD4<sup>+</sup> and CD8<sup>+</sup> T cell subtypes (Extended Data Fig. 1d). T cells responding to SARS-CoV-2 antigens had a memory phenotype, compatible with priming during infection with related coronaviruses (Extended Data Fig. 1e,f). Frequencies of spike-antigen-reactive T cells were twice as high as nucleocapsid-reactive T cells, and only spike protein stimulation induced significantly higher responses in controls than in patients with CAD (Extended Data Fig. 1g,h).

To test whether this impaired antigen response was specific for SARS-CoV-2 protein or had relevance for other viral antigens, we examined T cell responses to the EBV glycoprotein gp350. The EBV glycoprotein outperformed the SARS-CoV-2 antigen and induced an average of 559.2 pg ml<sup>-1</sup> of IFN- $\gamma$  in healthy responders (Fig. 1d). Again, the cells from patients with CAD failed to reach similar IFN- $\gamma$  production, yielding only about 240 pg ml<sup>-1</sup> (Fig. 1d). After 5 days of EBV antigen stimulation, healthy individuals recruited 3.27% of CD69<sup>+</sup>CD40L<sup>+</sup> T cells, almost two-fold-higher frequencies than the 1.77% in patients with CAD (Fig. 1e).

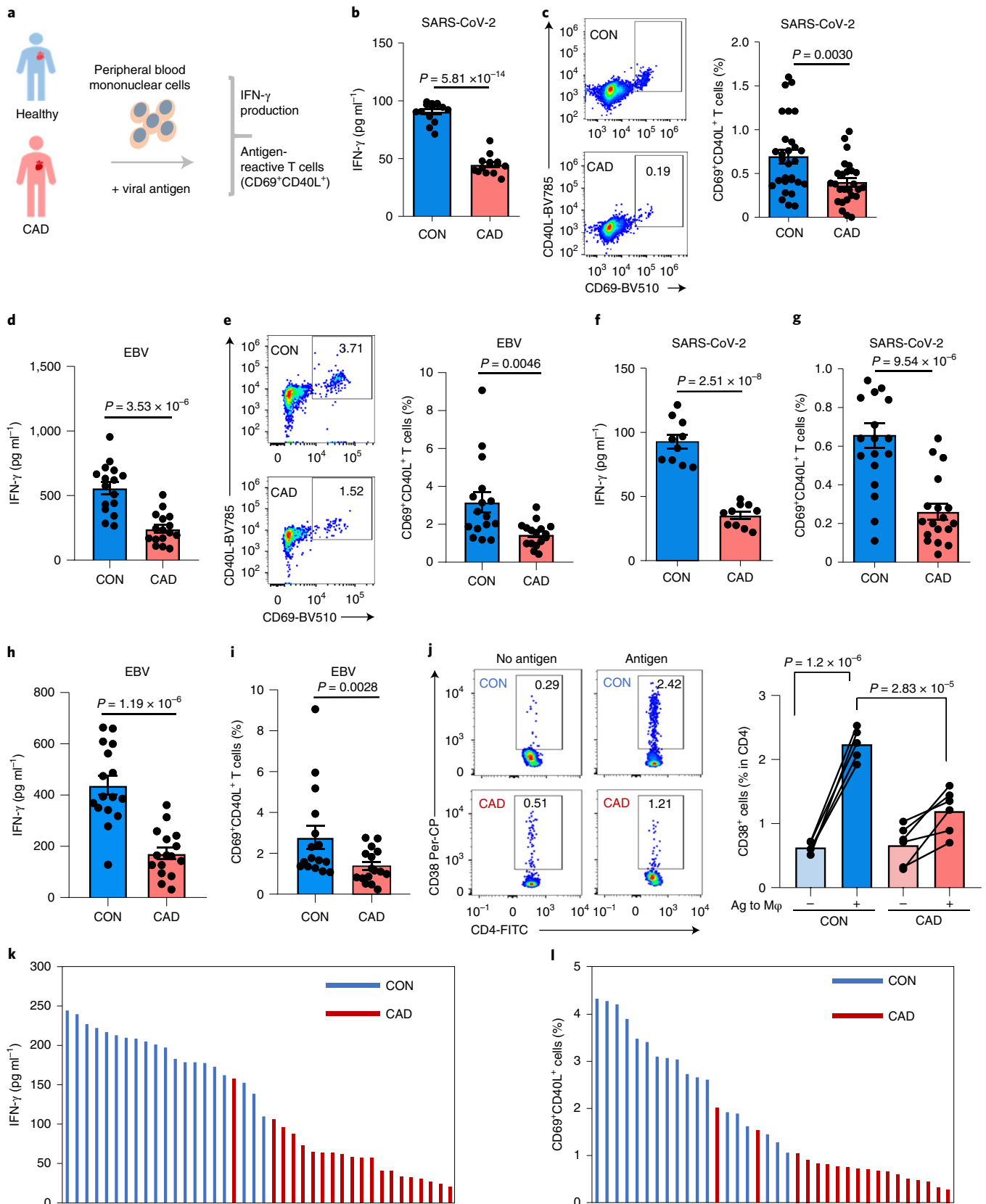
We tested whether improved antigen presentation could overcome defective T cell responsiveness by pre-loading fully differentiated M $\phi$  with S antigen. Pre-loaded M $\phi$  provoked robust IFN- $\gamma$  production in healthy T cells but elicited a blunted reaction in patient-derived T cells (Fig. 1f). Healthy individuals generated an excellent recall response, whereas CAD T cells failed to expand (Fig. 1g). Healthy M $\phi$  pre-loaded with EBV antigen induced strong IFN- $\gamma$  release, unmatched by the patients (Fig. 1h). Patients recalled EBV-specific T cells at about 50% of the frequencies encountered in healthy controls (Fig. 1i).

To establish relevance of these observations for *in vivo* anti-viral immunity, we investigated anti-SARS-CoV-2 T cell responses in immunodeficient NSG mice. NSG mice were reconstituted with T cells and macrophages from either healthy individuals or patients with CAD (Extended Data Fig. 2a) and immunized with viral protein. Adoptive transfer of antigen-loaded M $\phi$  prompted expansion of a population of CD4<sup>+</sup>CD38<sup>+</sup> T cells in the spleen (Fig. 1j and Extended Data Fig. 2b,c). Direct comparison of CD4<sup>+</sup>CD38<sup>+</sup> T cell frequencies induced by antigen-loaded and vehicle-loaded M $\phi$  established specificity of the response. Mice reconstituted with healthy T cells and injected with antigen-carrying M $\phi$  accumulated 2.24% of CD4<sup>+</sup>CD38<sup>+</sup> T cells in their spleen. In contrast, chimeras reconstituted with CAD T cells mobilized only 1.19% of CD4<sup>+</sup>CD38<sup>+</sup> T cells (Fig. 1j).

**Fig. 1 | Blunted anti-viral T cell responses in patients with CAD.** **a**, Experimental design. PBMCs were stimulated with viral protein antigens (1  $\mu$ g ml<sup>-1</sup>) for 5 days. **b,c**, PBMCs were stimulated with SARS-CoV-2 spike and nucleocapsid antigens for 5 days. IFN- $\gamma$  was quantified in supernatants (**b**,  $n = 15$ ). Frequencies of CD4<sup>+</sup>CD69<sup>+</sup>CD40L<sup>+</sup> T cells were measured in 29 controls and 26 patients. Representative dot plots and summary data are shown (**c**). **d,e**, PBMCs were stimulated with EBV glycoprotein 350 for 5 days. IFN- $\gamma$  concentrations (**d**) and frequencies of CD4<sup>+</sup>CD69<sup>+</sup>CD40L<sup>+</sup> T cells (**e**). Representative dot plots and summary data are presented ( $n = 16$  patients and  $n = 16$  controls). **f,g**, T cells were primed with viral antigens for 5 days and restimulated with autologous antigen-loaded monocyte-derived M $\phi$ . IFN- $\gamma$  release (**f**,  $n = 10$  patients and controls) and frequencies of CD69<sup>+</sup>CD40L<sup>+</sup> T cells (**g**,  $n = 18$  patients and  $n = 19$  controls) in response to SARS-CoV-2 antigen-loaded M $\phi$ . **h,i**, Antigen-induced IFN- $\gamma$  release and frequencies of CD69<sup>+</sup>CD40L<sup>+</sup> T cells in response to M $\phi$  loaded with EBV antigen ( $n = 16$  patients and  $n = 16$  controls). **j**, Frequencies of CD4<sup>+</sup>CD38<sup>+</sup> human T cells in the spleen of immuno-deficient mice that were reconstituted with patient-derived or control PBMCs and immunized with SARS-CoV-2 spike protein ( $n = 6$  patients and  $n = 5$  controls). **k,l**, T cell responses to SARS-CoV-2 spike protein in patients and controls who had completed vaccination with an mRNA-based COVID-19 vaccine. IFN- $\gamma$  secretion and frequencies of antigen-reactive CD69<sup>+</sup>CD40L<sup>+</sup> T cells. Individual data points are displayed. Data in Fig. 1b–j are shown as mean  $\pm$  s.e.m. Paired or unpaired one-way ANOVA were used to analyze the difference. *P* values are shown in each panel. CON, control.

The Pfizer-BioNTech (BNT162b2) and Moderna (mRNA-1273) mRNA COVID-19 vaccines induce measurable T cell responses to spike protein<sup>28,29</sup>. To examine whether COVID-19 vaccination can assist patients with CAD to generate adequate T cell immunity to

SARS-CoV-2 antigens, we recruited fully vaccinated healthy controls and patients with CAD. Strikingly, IFN- $\gamma$  production was twice as high in the vaccinated compared to the non-vaccinated healthy individuals (Fig. 1k). Also, spike-reactive CD69<sup>+</sup>CD40L<sup>+</sup>



T cells reached ~3% of CD4<sup>+</sup> T cells, three-fold higher than the ~1% frequencies measured in non-vaccinated healthy donors (Fig. 1l). Vaccination with the mRNA-based vaccines did not significantly change the frequency of anti-SARS-CoV-2-reactive T cells in patients with CAD. Vaccination slightly, but non-significantly, boosted IFN- $\gamma$  production (Fig. 1k). In a cohort of 20 post-vaccine patients with CAD, 17 patients had frequencies of spike-induced CD69<sup>+</sup>CD40L<sup>+</sup> T cells of less than 1% (Fig. 1l).

Together, these data identified a population of IFN- $\gamma$ -producing CD4<sup>+</sup> memory T cells that proliferated when recognizing viral antigens. In patients with CAD, anti-viral CD4<sup>+</sup> T cells were poorly responsive to SARS-CoV-2 and EBV antigens, and vaccination with an mRNA-based vaccine could not overcome the defect.

**CAD M $\phi$  overexpress the immunoinhibitory ligand CD155.** The intensity and durability of antigen-specific T cell responses depends on antigen recognition but is critically influenced by the co-stimulatory and co-inhibitory signals delivered by the antigen-presenting cell<sup>30</sup>. We profiled the transcriptome of M $\phi$  derived from patients and controls for 12 co-stimulatory and co-inhibitory molecules (Fig. 2a and Extended Data Fig. 4a). Transcripts for *PD-L1* and *PVR* were significantly increased in CAD M $\phi$ , but *PVR* displayed the most robust difference. Flow cytometric analysis of control and CAD M $\phi$  confirmed high surface expression of CD155 (Fig. 2b). Confocal imaging of CD155 demonstrated high expression of the protein in the cytoplasm and on the cell surface in CAD M $\phi$  (Fig. 2c). We explored whether M $\phi$  residing in the atherosclerotic plaque have a CD155<sup>hi</sup> phenotype. Dual color immunohistochemistry of atheroma tissue placed CD155 exclusively on CD68<sup>+</sup> M $\phi$  (Fig. 2d). Plaque-residing M $\phi$  are a heterogeneous population<sup>18</sup>. To understand which M $\phi$  subtypes express CD155, we digested the atherosclerotic arteries and used multi-parametric flow cytometry to define relevant cell populations (Extended Data Fig. 3a). Based on the expression pattern of the antigen-presenting molecule HLA-DR and the M $\phi$  marker CD206, tissue-derived CD45<sup>+</sup> CD68<sup>+</sup> cells fell into four clusters, two of which expressed HLA-DR and were, therefore, capable of antigen presentation (Extended Data Fig. 3b). HLA-DR<sup>hi</sup>CD206<sup>neg</sup> and HLA-DR<sup>int</sup>CD206<sup>pos</sup> tissue M $\phi$  were both strongly positive for CD155 (Extended Data Fig. 3c). Conversely, HLA-DR<sup>neg</sup> tissue M $\phi$ , including a CD206<sup>pos</sup> and CD206<sup>neg</sup> population, lacked CD155 expression. Accordingly, polarization of monocyte-derived CAD M $\phi$  with either lipopolysaccharide (LPS) plus IFN- $\gamma$  (M1-like M $\phi$ ) or IL-4 (M2-like M $\phi$ ) aligned CD155 expression to the pro-inflammatory phenotype (Extended Data Fig. 3d).

To define the functional effect of CD155<sup>hi</sup> expression on CAD M $\phi$ , we analyzed whether the abundance of CD155 on M $\phi$  has relevance for anti-viral T cell immunity. CD155 expression on the M $\phi$  surface negatively correlated with antigen-induced IFN- $\gamma$  production (Fig. 2e). Furthermore, we suppressed CD155-dependent

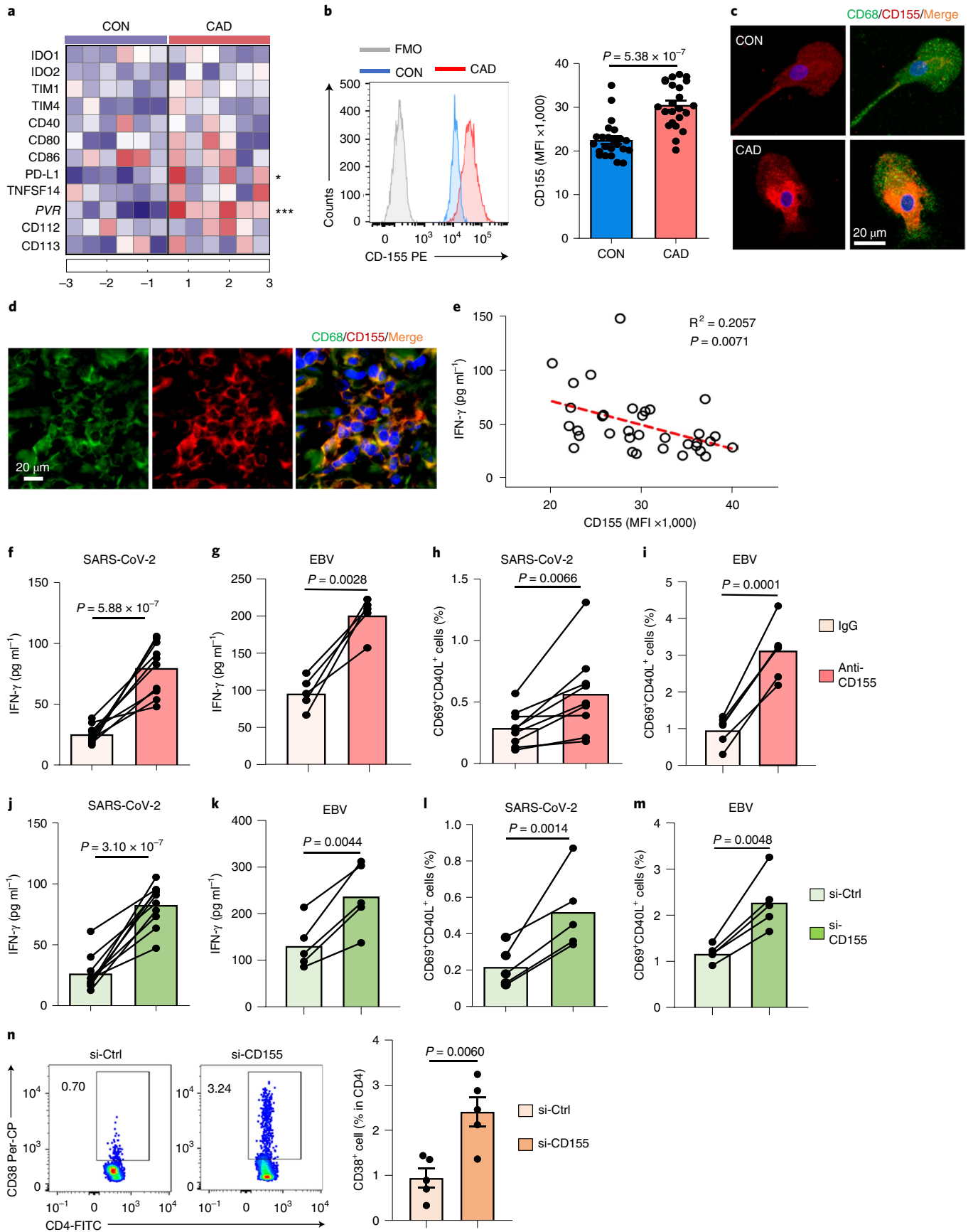
signaling through CD155-blocking antibodies or by CD155 knock-down (Extended Data Fig. 4b,c). T cells responding to viral antigens were quantified as the measure of functional outcome. Both strategies successfully restored the ability of CAD M $\phi$  to activate anti-viral T cells (Fig. 2f–m). Blocking CD155 on patient M $\phi$  restored antigen-presenting function, but CD155 blockade of healthy M $\phi$  had no effect on T cell responsiveness (Extended Data Fig. 4d–k). For both, SARS-CoV-2 and EBV antigens, anti-CD155-blocking antibodies improved antigen-induced IFN- $\gamma$  production to the level of normal controls (Figs. 2f,g) and brought CAD T cell yield into the normal range (Fig. 2h,i). Knockdown of CD155 was similarly successful, normalizing the frequencies of IFN- $\gamma$  release and CD4<sup>+</sup>CD69<sup>+</sup> CD40L<sup>+</sup> T cells (Fig. 2j–m).

To expand these findings to in vivo conditions, we injected NSG mice with CAD M $\phi$ , T cells and SARS-CoV-2 antigen (Extended Data Fig. 2a). CD155 knockdown in M $\phi$  before the adoptive transfer enhanced the activation and expansion of antigen-reactive T cells more than four-fold (Fig. 2n). Both ex vivo and in vivo, correcting CD155 overexpression was sufficient to restore CD4<sup>+</sup> T cell reactivity against SARS-CoV-2 antigen to a level seen in healthy controls. These data implicated the immunoinhibitory ligand CD155 in suppressing anti-viral T cell immunity and mapped the immune defect in patients with CAD to M $\phi$ .

**Inhibitory receptors of CD155 accumulate on memory T cells.** CD155 delivers a negative signal to T cells by binding to the ITIM motif-containing receptors TIGIT and CD96 (ref. 16). To identify T cells capable of recognizing CD155, we analyzed CD4<sup>+</sup> memory T cell populations for the expression of TIGIT and CD96. Naive CD4<sup>+</sup> T cell and resting CD4<sup>+</sup> memory populations were essentially negative for both receptors (Fig. 3a,b). T cell receptor-mediated stimulation resulted in robust upregulation of TIGIT and CD96 transcripts and protein (Fig. 3a–e), starting 72 hours after stimulation.

To analyze the expression patterns of receptors mediating inhibitory signals, we used multi-parametric flow cytometry for CD96, TIGIT, PD-1 and CD226 on stimulated CD4<sup>+</sup> memory T cells from patients and controls. Uniform manifold approximation and projection (UMAP) plots revealed partly overlapping expression of TIGIT and CD96 on activated T cells. Besides the CD4<sup>+</sup>TIGIT<sup>+</sup>CD96<sup>+</sup> T cell subset, we found a subpopulation of TIGIT<sup>+</sup>CD96<sup>neg</sup> cells (Fig. 3c,d). CD4<sup>+</sup>TIGIT<sup>+</sup>CD96<sup>-</sup> T cells and CD4<sup>+</sup>CD96<sup>+</sup>TIGIT<sup>+</sup> double-positive T cells accounted for about 15% on day 3 and 20% on day 5 (Fig. 3c,d). Some of the TIGIT<sup>+</sup>CD96<sup>+</sup> cells also expressed PD-1 (Fig. 3e). In contrast, CD226<sup>+</sup> T cells belonged to a separate cluster (Fig. 3f). Thus, about one-fourth of the memory T cell population possesses receptors capable of interacting with CD155, being susceptible to negative signaling delivered by CD155<sup>hi</sup>-expressing M $\phi$ . The distributions of CD4<sup>+</sup> T cell clusters expressing CD96, TIGIT, PD-1 and CD226 were indistinguishable in patients and controls.

**Fig. 2 | CD155<sup>hi</sup> macrophages suppress anti-viral T cell responses.** **a–c**, Monocyte-derived M $\phi$  were generated from patients and controls. Gene expression signature for 14 immune checkpoint genes in healthy and CAD M $\phi$  ( $n=6$ ). qPCR results are shown as a heat map (**a**). Flow cytometry of CD155 surface expression in healthy and CAD M $\phi$ . Representative histograms and summary data from  $n=27$  controls and  $n=27$  patients are shown (**b**). Confocal immunofluorescence of CD155 protein expression in healthy and CAD M $\phi$ . Representative images from three independent experiments (**c**). **d**, Fluorescence microscopy of atherosclerotic plaque tissue sections stained for CD68 (green) and CD155 (red). Representative images from four experiments. **e**, Correlation of antigen-induced IFN- $\gamma$  release and M $\phi$  CD155 expression in  $n=34$  patients with CAD. **f,g**, IFN- $\gamma$  secretion after SARS-CoV-2 antigen (**f**,  $n=10$ ) or EBV antigen (**g**,  $n=5$ ) stimulation in the absence or presence of anti-CD155 antibodies. **h,i**, Frequencies of CD69<sup>+</sup>CD40L<sup>+</sup> T cells induced by SARS-CoV-2 antigen (**h**,  $n=8$ ) or EBV antigen (**i**,  $n=5$ ) stimulation with and without CD155 blockade. **j–m**, M $\phi$  were transfected with control or CD155 siRNA before antigen loading. IFN- $\gamma$  induction after stimulation with SARS-CoV-2 antigen (**j**,  $n=10$ ) or EBV antigen (**k**,  $n=5$ ). Frequencies of SARS-CoV-2-reactive CD69<sup>+</sup> CD40L<sup>+</sup> T cells (**l**,  $n=6$ ) and EBV-reactive CD69<sup>+</sup>CD40L<sup>+</sup> T cells (**m**,  $n=5$ ). **n**, In vivo anti-SARS-CoV-2 T cell responses were measured in immunodeficient NSG mice that were reconstituted with human PBMCs and immunized with viral protein. M $\phi$  were transfected with control or CD155 siRNA before the adoptive transfer. After 1 week, antigen-induced human CD4<sup>+</sup>CD38<sup>+</sup> T cells were measured in the spleen. Representative dot blots of CD4<sup>+</sup>CD38<sup>+</sup> T cells and frequencies of CD4<sup>+</sup>CD38<sup>+</sup> T cells. Data are from five experiments. Data are mean  $\pm$  s.e.m. Comparison by one-way ANOVA. Correlation analysis with linear regression.  $P$  values are shown in each panel. CON, control; FMO, Fluorescence Minus One; MFI, mean fluorescence intensity.



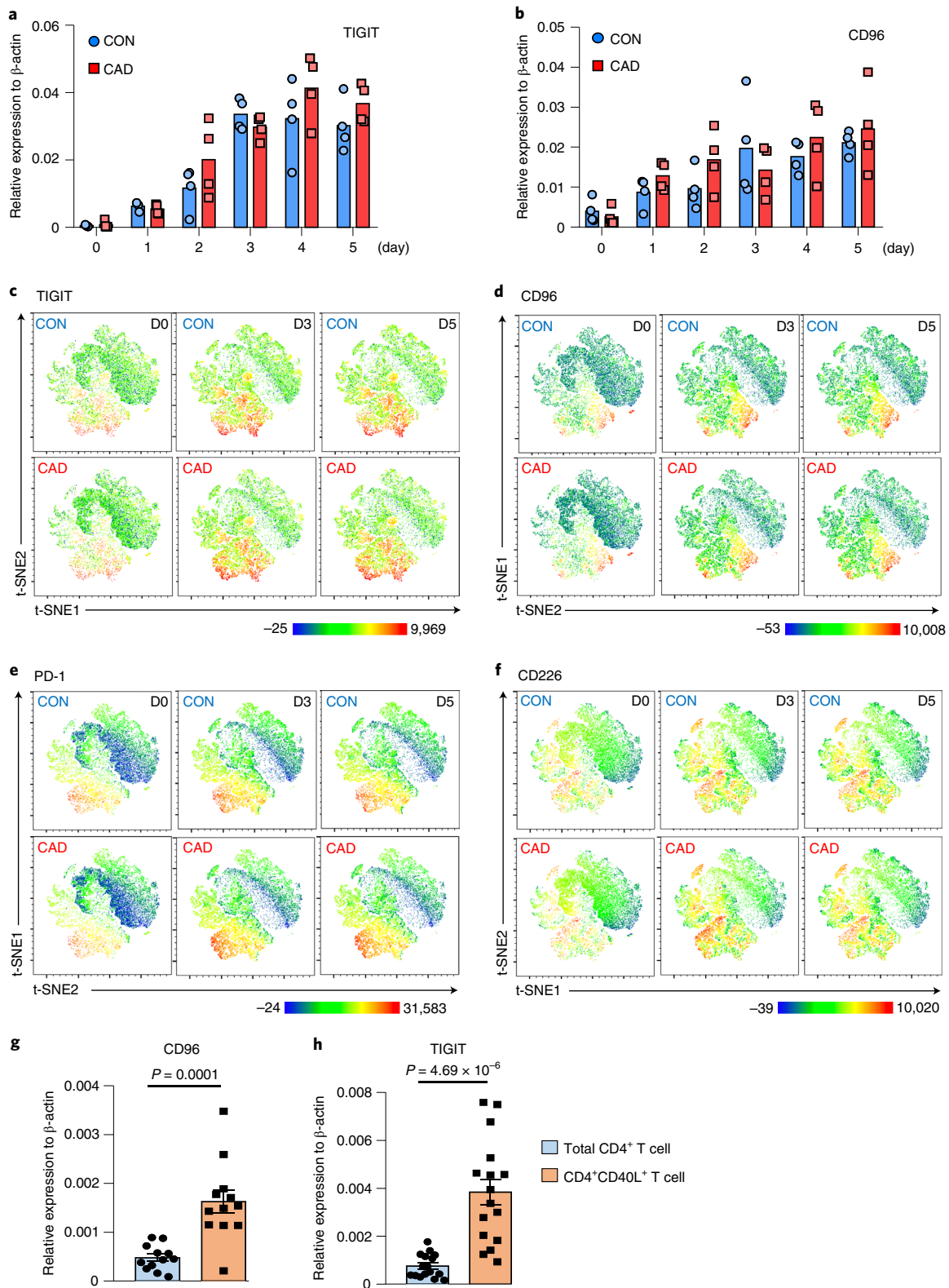


**Fig. 3 | Expression of the CD155 receptors TIGIT and CD96 on activated memory CD4<sup>+</sup> T cells.** **a-d**, CD4<sup>+</sup>CD45RO<sup>+</sup> memory T cells isolated from healthy individuals and patients with CAD were stimulated with anti-CD3/anti-CD28 for 5 days. Kinetics of TIGIT (**a**) and CD96 (**b**) transcript expression measured by RT-PCR ( $n = 4$  patients and  $n = 4$  controls). UMAP clustering of multi-parametric flow cytometry data. The expression of the co-inhibitory receptors TIGIT (**c**), CD96 (**d**), PD-1 (**e**) and CD226 (**f**) is indicated. Each dot plot concatenates data from six experiments. **g,h**, PBMCs were stimulated with SARS-CoV-2 proteins ( $1 \mu\text{g ml}^{-1}$ ) for 5 days. Total CD4<sup>+</sup> T cells and antigen-reactive CD40L<sup>+</sup> T cells were isolated, and TIGIT (**g**,  $n = 12$ ) and CD96 (**h**,  $n = 16$ ) transcripts were measured by RT-PCR. Data are mean  $\pm$  s.e.m. Comparison by one-way ANOVA.  $P$  values are shown in each panel. CON, control; D, day.

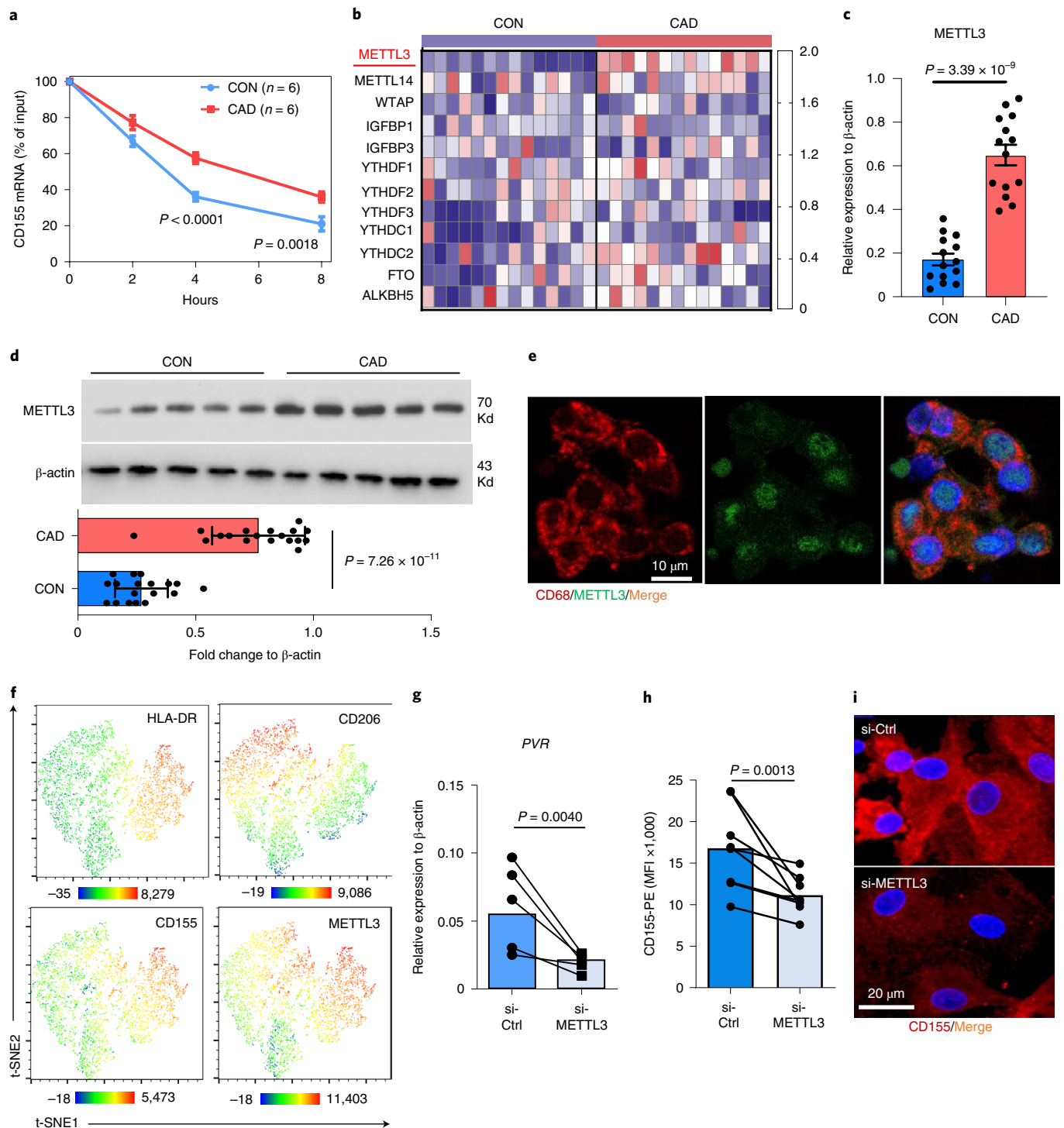


**Fig. 4** | N<sup>6</sup>-adenosine-methyltransferase METTL3 stabilizes PVR mRNA in CAD M $\phi$ . **a–d**, Monocyte-derived M $\phi$  were generated from controls and patients with CAD. PVR mRNA was quantified after treatment with the transcription inhibitor actinomycin D ( $3 \mu\text{g ml}^{-1}$ ; 0–8 hours) (**a**,  $n = 6$ ). Transcripts of 12 m<sup>6</sup>A-related genes measured by RT-PCR. Data shown as heat maps (**b**,  $n = 14$ ). RT-PCR quantification of METTL3 transcripts (**c**,  $n = 14$ ). Immunoblotting of METTL3 protein.  $\beta$ -actin served as control. Representative blot and data from 18 patients and 18 controls (**d**). **e**, METTL3 (green) in CD68<sup>+</sup> tissue-residing M $\phi$  (red) in atherosclerotic plaque tissue sections. Representative images from four experiments. **f**, t-SNE clustering of multi-parametric flow cytometry data from M $\phi$  isolated from human atherosclerotic arteries. Expression patterns of HLA-DR, CD206, CD155 and METTL3 indicated by color code. Each dot plot concatenates data from two tissues. **g–i**, siRNA-mediated METTL3 knockdown in control and CAD M $\phi$ . CD155 transcripts measured by RT-PCR (**g**,  $n = 5$ ). CD155 surface expression analyzed by flow cytometry (**h**,  $n = 8$ ). Confocal immunofluorescence staining for CD155 (red). Images are representative of three independent experiments (**i**). Each point represents one patient or one healthy control. Data are mean  $\pm$  s.e.m. Comparison by two-tailed unpaired Student's *t*-test (**b,d**) and two-tailed paired Student's *t*-test (**g,h**). *P* values are shown in each panel. CON, control.

We asked whether CD4<sup>+</sup> T cells activated by viral protein fell into the TIGIT<sup>+</sup>CD96<sup>+</sup> subset, thus being receptive to the inhibitory signals from CD155<sup>hi</sup> Mφ. We sorted CD40L<sup>+</sup> T cells after SARS-CoV-2 antigen stimulation for 5 days. Total CD4<sup>+</sup> T cells were purified to serve as a control. *TIGIT* and *CD96* transcripts were highly enriched among antigen-reactive, CD40L-expressing T cells, with three-fold- or four-fold-higher prevalence compared to the overall CD4<sup>+</sup> T cell pool (Fig. 3g,h). Thus, antigen stimulation upregulates the inhibitory receptors CD96 and TIGIT in CD4<sup>+</sup> T cells, rendering them vulnerable to negative signaling from CD155<sup>+</sup> antigen-presenting cells.

#### N<sup>6</sup>-methyltransferase METTL3 stabilizes *PVR* mRNA in CAD Mφ.

To identify and characterize mechanisms underlying the CD155<sup>hi</sup> phenotype in CAD Mφ, we determined *PVR* mRNA stability through an actinomycin D-dependent RNA decay assay<sup>31</sup>. *PVR* mRNA turnover was high, with half of the transcripts being degraded within 3–4 hours (Fig. 4a). In CAD Mφ, the half-life of *PVR* mRNA was significantly prolonged, with 50% of transcripts still available after 6 hours, suggesting that CD155 overexpression on CAD Mφ was a consequence of increased RNA stability.

mRNA modifications have been implicated in regulating mRNA stability and fate<sup>21</sup>. Specifically, the most abundant mRNA modification, m<sup>6</sup>A, determines target mRNA concentrations by affecting RNA stability, decay and alternative splicing<sup>20</sup>. The m<sup>6</sup>A process is reversible and requires two different components: the ‘writer’ N<sup>6</sup>-methyltransferase complex, which catalyzes the formation of m<sup>6</sup>A, and the ‘eraser’ demethylase, which reverses the methylation. We profiled gene expression patterns for 12 common m<sup>6</sup>A-related genes, including ‘writers’, ‘readers’ and ‘erasers’ (Fig. 4b). Most genes were expressed at similar abundance in control and CAD Mφ, but transcripts for the writer METTL3, the only methylase in the N<sup>6</sup>-methyltransferase complex<sup>32</sup>, were significantly higher in CAD Mφ (Fig. 4c). Immunoblotting confirmed two-fold-higher protein concentrations of METTL3 in CAD compared to healthy Mφ (Fig. 4d). To evaluate METTL3 expression in tissue-residing Mφ within the atheroma, we applied dual-color immunohistochemistry. METTL3 was highly expressed in plaque-infiltrating CD68<sup>+</sup> Mφ. Most of the enzyme localized to the nucleus (Fig. 4e).

To understand the expression pattern of METTL3 in atherosclerotic arteries, we performed multi-parametric flow cytometry of Mφ isolated from atherosclerotic arteries (Extended Data Fig. 3a). Again, HLA-DR<sup>hi</sup>CD206<sup>neg</sup> and HLA-DR<sup>int</sup>CD206<sup>pos</sup> tissue Mφ stained strongly positive for METTL3 (Extended Data Fig. 6a). t-distributed stochastic neighbor embedding (t-SNE) visualization of plaque-residing Mφ confirmed the overlap of METTL3, CD155 and HLA-DR expression on CD206<sup>neg</sup> Mφ (Fig. 4f), assigning antigen presentation to Mφ recognized for their pro-inflammatory features<sup>33</sup>.

To mechanistically connect METTL3-dependent m<sup>6</sup>A to CD155 mRNA stability, we used siRNA technology to knock down Mφ METTL3 (Extended Data Fig. 6b,c). Culturing of Mφ and knockdown of METTL3 did not make a difference in the survival of Mφ between groups (Extended Data Fig. 5a–h). Reducing METTL3 availability promptly lowered Mφ *PVR* mRNA concentrations (Fig. 4g) and protein expression (Fig. 4h and Extended Data Fig. 6d). Confocal imaging of Mφ transfected with control or METTL3 siRNA confirmed the dependency of CD155 expression on the methyltransferase (Fig. 4i). Similarly, treating Mφ with the m<sup>6</sup>A inhibitor 3-deazaadenosine (3-DAA) led to a reduction of CD155 transcript level and protein accumulation in Mφ (Extended Data Fig. 6e,f).

The m<sup>6</sup>A modification is most likely to occur in a DRACH (D = A, G or U; H = A, C or U) consensus motif. To identify potential DRACH sites in *PVR* mRNA, we analyzed the CD155 sequence with the m<sup>6</sup>A prediction server SRAMP<sup>34</sup> and searched m<sup>6</sup>A RNA immunoprecipitation (Me-RIP) sequence data obtained from the human monocytic cell lines monomac-6 (GSE76414 (ref. 35)) and

nomo-1 (GSE87190 (ref. 36)), yielding six potential sites with high confidentiality scores (Extended Data Fig. 6g and Supplementary Table 1). All six DRACH sites were localized in the 3′ untranslated region (UTR) of *CD155* mRNA (Fig. 5a). To interrogate site-specific m<sup>6</sup>A, we applied an RT-PCR-based system<sup>37</sup> that relies on the m<sup>6</sup>A-dependent suppression of retro-transcription with Bst enzyme but not with MRT enzyme (Fig. 5a). This approach mapped highly methylated sites to positions 1635A and 3103A of *CD155* mRNA in CAD Mφ (Fig. 5b,c). Site-specific mutations followed by dual luciferase reporter assays provided strong support for functional relevance of m<sup>6</sup>A modification at the two positions (Fig. 5d). Luciferase activity for a reporter carrying the *CD155* 3′ UTR wild-type region was higher in patient-derived versus healthy Mφ. After the two m<sup>6</sup>A sites were mutated, luciferase activity was indistinguishable in control and CAD Mφ (Fig. 5e,f). *METTL3* knockdown in CAD Mφ eliminated the difference in luciferase activity, confirming the relevance of methylation in controlling *CD155* mRNA expression (Figs. 4h and 5g).

To further evaluate the contribution of m<sup>6</sup>A modification on *PVR* mRNA stability, we performed a Me-RIP assay using m<sup>6</sup>A capture antibodies (Extended Data Fig. 6h). In healthy Mφ, the m<sup>6</sup>A modification of *PVR* mRNA was barely detectable (Fig. 5i). In contrast, m<sup>6</sup>A capture antibodies successfully pulled down *PVR* mRNA in CAD Mφ (Extended Data Fig. 6i). Capture with IgG isotype control antibodies yielded no differences in *PVR* mRNA pulldown (Extended Data Fig. 6i). Knockdown of *METTL3* in patient-derived Mφ eliminated the enrichment of m<sup>6</sup>A-modified *PVR* mRNA (Fig. 5j and Extended Data Fig. 6j). Suppressing m<sup>6</sup>A generation by either using the m<sup>6</sup>A inhibitor 3-DAA or knocking down *METTL3* effectively accelerated the decay of *PVR* RNA (Fig. 5k). These data identified *METTL3* as a regulator of *PVR* mRNA stability and implicated m<sup>6</sup>A RNA methylation in determining the antigen-presenting capacity of Mφ.

**METTL3 controls anti-viral T cell responses.** Association of the METTL3<sup>hi</sup>CD155<sup>hi</sup> phenotype in CAD Mφ with impaired anti-SARS-CoV-2 T cell responses raised the question of whether *METTL3* ultimately controls the intensity and intactness of adaptive anti-viral immunity. Correlative studies indicated that the amount of *METTL3* protein in Mφ negatively correlated with the release of anti-viral IFN-γ in each patient tested (Fig. 6a). To examine the role of *METTL3*-dependent m<sup>6</sup>A in regulating the antigen-presenting function of Mφ, we quantified the induction of anti-viral T cells before and after *METTL3* knockdown. Reducing the concentration of *METTL3* mRNA by 50% in healthy Mφ had no effect on the expansion of both SARS-CoV-2-responsive and EBV-responsive T cells (Extended Data Fig. 7a–d) in the in vitro antigen presentation assay. In contrast, transfection of CAD Mφ with *METTL3* siRNA profoundly changed the ability of these Mφ to present viral proteins and stimulate T cells (Fig. 6b–e). *METTL3* knockdown disrupted the immunoinhibitory function of CAD Mφ and increased both the production of IFN-γ (Fig. 6b,c) and the frequency of CD40L<sup>+</sup>CD69<sup>+</sup>CD4<sup>+</sup> T cells (Fig. 6d,e) in cultures primed with both viral antigens. Treatment of antigen-presenting Mφ with the m<sup>6</sup>A inhibitor 3-DAA normalized antigen responsiveness and IFN-γ release of patient-derived T cells (Fig. 6f–i) but did not make a difference in control cells (Extended Data Fig. 7e–h). The beneficial effects of inhibiting the methyltransferase activity of *METTL3* were maintained in vivo. Suppression of m<sup>6</sup>A modification in Mφ through *METTL3* knockdown before their adoptive transfer restored the induction of antigen-driven T cell responses indicated by the expansion of CD4<sup>+</sup>CD38<sup>+</sup> T cells in the spleens of antigen-immunized NSG mice (Fig. 6j). Taken together, these data indicate that excess methylation of *PVR* mRNA due to inappropriate expression of the methyltransferase *METTL3* weakens the induction of antigen-specific T cells and undermines host protective immune responses against viral antigens.

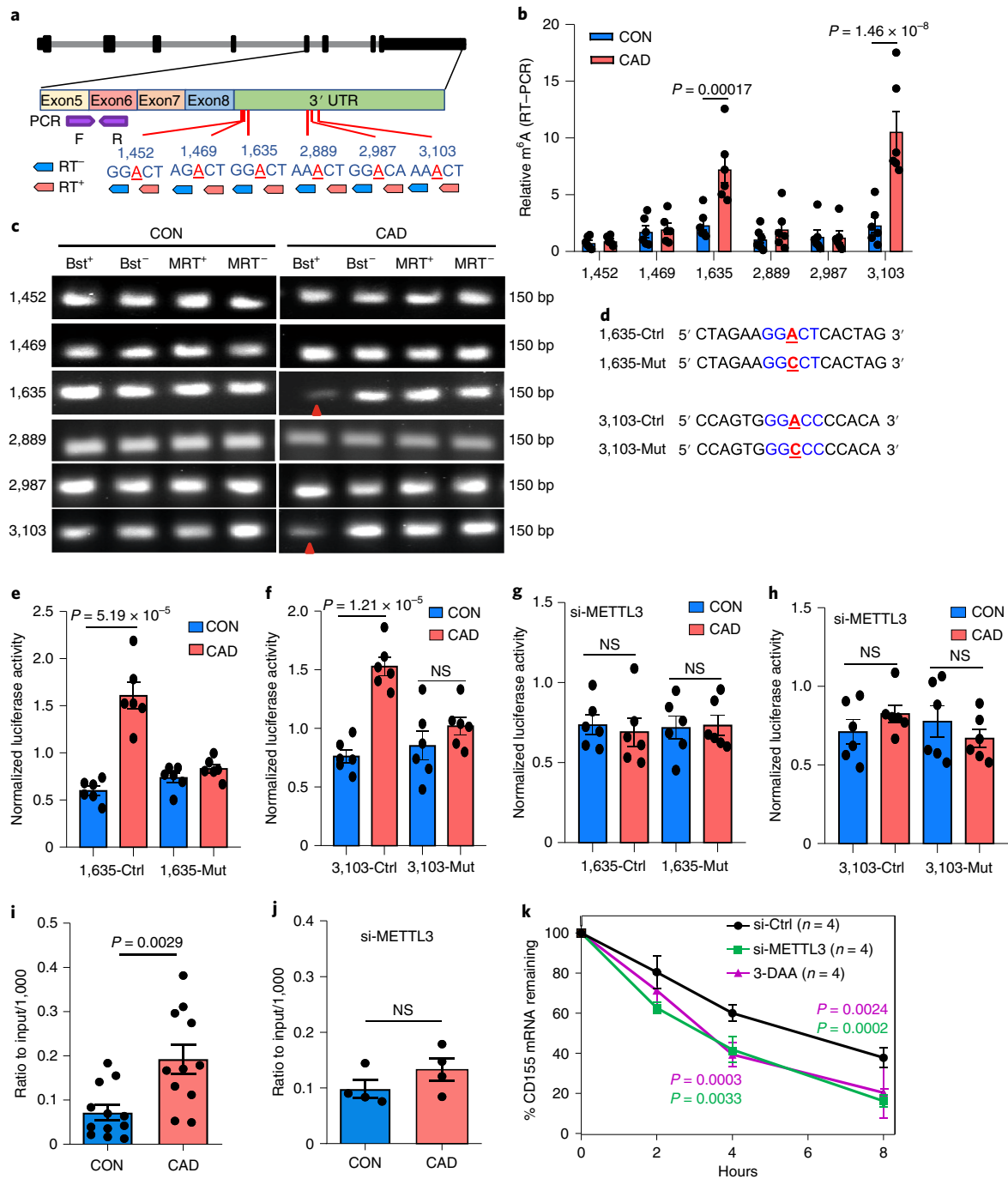


**Fig. 5 | m<sup>6</sup>A modification on 1635A and 3103A enhances the stability of PVR mRNA.** **a**, Scheme of *PVR* genomic organization, potential m<sup>6</sup>A sites, strategy of retro-transcription and RT-PCR for mapping of m<sup>6</sup>A sites. **b,c**, PCR of retro-transcribed M $\phi$  RNA using m<sup>6</sup>A<sup>+</sup> and m<sup>6</sup>A<sup>-</sup> primers and BstI and MRT enzymes. m<sup>6</sup>A-RT-PCR for different m<sup>6</sup>A sites on *CD155* transcripts (**b**,  $n = 6$ ). Representative agarose gel electrophoresis of PCR products for different m<sup>6</sup>A sites on *PVR* transcripts (**c**). **d**, Design of the m<sup>6</sup>A point mutations in the 3' UTR of *PVR*. **e,f**, Dual luciferase reporter assays for m<sup>6</sup>A sites in the 3' UTR of *PVR*. Site 1635A (**e**) and site 3103A (**f**) ( $n = 6$ ). **g,h**, Dual luciferase reporter assays for m<sup>6</sup>A sites in the 3' UTR of *PVR* after *METTL3* knockdown. Site 1635A (**g**) and site 3103A (**h**) ( $n = 6$ ). **i,j**, Methylated RNA immunoprecipitation (Me-RIP) assay to quantify m<sup>6</sup>A. Methylated *CD155*-specific mRNA in control and CAD M $\phi$  measured by Me-RIP (**i**,  $n = 12$ ). Methylated *PVR* mRNA determined by Me-RIP after siRNA-mediated *METTL3* knockdown (**j**,  $n = 4$ ). **k**, *PVR* mRNA decay assay in M $\phi$  treated with the m<sup>6</sup>A inhibitor 3-DAA or transfected with *METTL3* siRNA ( $n = 4$ ). Each point represents one patient or one healthy control. Data are mean  $\pm$  s.e.m. Comparisons by unpaired Student's *t*-test (**b,i,j**), one-way ANOVA (**e-h**) and two-way ANOVA (**k**). *P* values are shown in each panel. bp, base pair; CON, control; F, forward; NS, not significant; R, reverse.

**Low-density lipoprotein induces the METTL3<sup>hi</sup>CD155<sup>hi</sup> phenotype in CAD monocytes.** The METTL3<sup>hi</sup>CD155<sup>hi</sup> phenotype is shared by ex vivo differentiated M $\phi$  and tissue-residing M $\phi$  in the atherosclerotic plaque. To explore how and when end-differentiated

M $\phi$  are reprogrammed to overexpress METTL3, we examined bone-marrow-derived circulating CD14<sup>+</sup> monocytes. Transcriptomic and flow cytometric analysis confirmed the CD155<sup>hi</sup> phenotype in CD14<sup>+</sup> CAD monocytes (Extended Data Fig. 8a–c). Also, CD14<sup>+</sup>

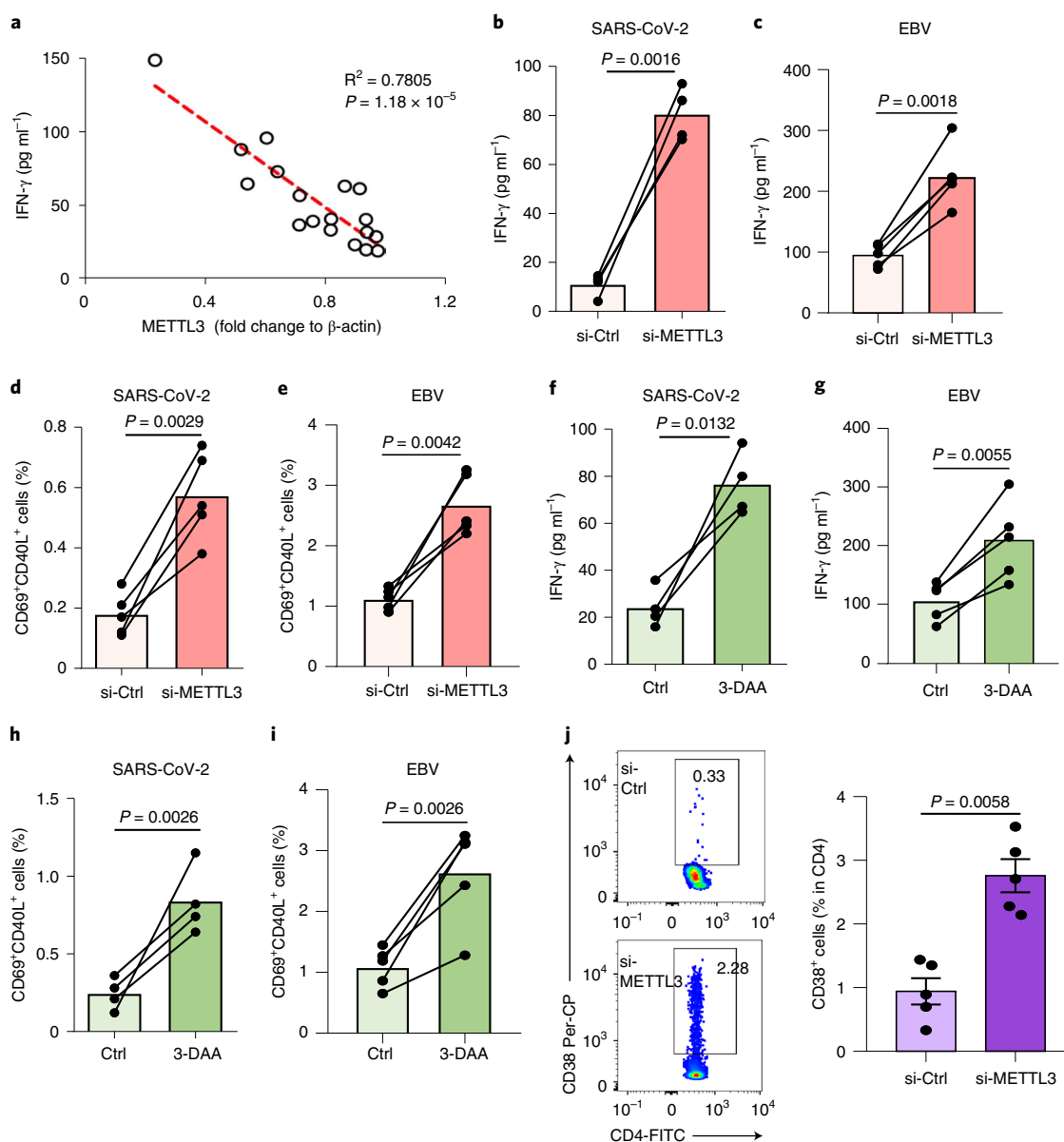


**Fig. 6 | Suppressing N<sup>6</sup>-adenosine modification of PVR mRNA restores anti-viral T cell responses.** **a**, SARS-CoV-2 antigen-induced T cell responses were analyzed as described in Fig. 1. Correlation of antigen-induced IFN- $\gamma$  released by T cells and the protein level of METTL3 in M $\phi$  from  $n = 18$  patients with CAD. **b–e**, METTL3 was knocked down in M $\phi$  by siRNA technology before examining their ability to induce T cell responses. IFN- $\gamma$  release in response to SARS-CoV-2 antigen (**b**) and EBV antigen (**c**) stimulation was measured in 4–5 experiments. Frequencies of SARS-CoV-2-specific CD69 $^{+}$ CD40L $^{+}$ CD4 $^{+}$  T cells (**d**) and EBV-specific CD69 $^{+}$ CD40L $^{+}$ CD4 $^{+}$  T cells (**e**) was measured in five experiments. **f–i**, CAD M $\phi$  were treated with the m<sup>6</sup>A inhibitor 3-DAA or vehicle. IFN- $\gamma$  release in response to SARS-CoV-2 antigen (**f**,  $n = 4$ ) and EBV antigen (**g**,  $n = 5$ ) stimulation was quantified. Frequencies of SARS-CoV-2-specific (**h**,  $n = 4$ ) and EBV-specific (**i**,  $n = 5$ ) CD69 $^{+}$ CD40L $^{+}$ CD4 $^{+}$  T cells measured by flow cytometry. **j**, To analyze the role of N<sup>6</sup>-adenosine-methyltransferase in anti-viral T cell responses in vivo, METTL3 was knocked down in CAD M $\phi$  before their transfer into NSG mice. Chimeras were immunized with SARS-CoV-2 antigen, and CD4 $^{+}$ CD38 $^{+}$  T cells were identified in the spleen.  $n = 5$  experiments. Individual data points are presented. Data are mean  $\pm$  s.e.m. Comparisons by one-way ANOVA. Correlation was analyzed by linear regression.  $P$  values are shown in each panel.

monocytes shared with M $\phi$  the METTL3<sup>hi</sup> phenotype, and immunoblotting demonstrated two-fold-higher amounts of METTL3 protein in patient-derived cells (Extended Data Fig. 8d,e). We determined PVR mRNA stability through an actinomycin D-dependent RNA decay assay (Extended Data Fig. 8f). The PVR mRNA half-life was significantly longer in CAD monocytes versus healthy controls. Quantification of m<sup>6</sup>A-modified PVR mRNA by Me-RIP assay demonstrated significant enrichment of PVR mRNA bound by the capture antibodies in patient-derived cells (Extended Data Fig. 8g). These results confirmed persistence of the reprogramming

process from precursor cells to mature M $\phi$  and guided the search for METTL3 inducers to the bone marrow environment.

In the first series of experiments, we explored whether serum lipids can induce CAD monocytes to acquire the METTL3<sup>hi</sup>CD155<sup>hi</sup> phenotype, similarly to the process in which bone marrow myeloid cells undergo epigenetic and functional changes that enhance immune activation upon re-exposure<sup>38</sup>. To mimic physiologic conditions, healthy monocytes were cultured in plasma samples with varying concentrations of low-density lipoprotein (LDL), high-density lipoprotein (HDL) and triglycerides (TGs). The priming effect

was assessed by quantifying *METTL3* and *PVR* mRNA transcripts after 48 hours. Correlative analysis between LDL and TG levels and transcript expression for *METTL3* and *PVR* pointed toward LDL as a possible ‘primer’, whereas plasma high in TGs failed to affect *METTL3* and *PVR* mRNA pools (Fig. 7a–d). In subsequent experiments, we used individual stimuli known to function as potent monocyte activators. Two stimuli effectively transformed healthy monocytes into *METTL3*<sup>hi</sup>*CD155*<sup>hi</sup> cells (Fig. 7e,f). Exposure to LDL and oxidized LDL (oxLDL) was sufficient to induce high abundance of both *METTL3* and *PVR* transcripts. There was a trend for LPS to function as an inducer of the two mRNAs, but all other stimuli were ineffective (Fig. 7e,f).

To investigate whether oxLDL regulates the ability of M $\phi$  to present viral antigens, we treated healthy M $\phi$  with oxLDL for 2 days before loading them with viral antigens. T cell reactivity to control and oxLDL-pre-treated antigen-presenting cells was assessed through IFN- $\gamma$  production (Fig. 7g,h) and mobilization of CD69<sup>+</sup>CD40L<sup>+</sup> T cells (Fig. 7i,j). oxLDL pre-treatment was sufficient to suppress T cell responses to both the SARS-CoV-2 antigen and the EBV antigen.

In summary, the reprogramming of CAD M $\phi$  begins early in their life cycle by affecting their precursor cells. A well-known metabolic abnormality in CAD—the increase in LDL and oxLDL—appears to have marked functional effect on antigen-presenting cells by altering mRNA methylation.

## Discussion

CAD is independently associated with an increased risk of in-hospital death among individuals infected with SARS-CoV-2, but mechanisms underlying the inability of patients with CAD to mount protective immune responses are poorly understood. By probing the competence of patients with CAD to mobilize T cell immunity against spike and nucleocapsid antigens, we have defined a defect in antigen presentation caused by inappropriate expression of the co-inhibitory ligand CD155. CD155<sup>hi</sup> CAD M $\phi$  engaged CD4<sup>+</sup>CD96<sup>+</sup> and CD4<sup>+</sup>TIGIT<sup>+</sup> memory T cells, delivering an inhibitory signal that essentially disrupted the clonal expansion of antigen-reactive CD4<sup>+</sup> T cells. Proliferative inhibition of anti-viral CD4<sup>+</sup> T cells extended to the release of IFN- $\gamma$ , a key protective factor in anti-viral immunity. We have defined the mechanisms underlying the functional reprogramming of CAD macrophages, rendering the defect druggable. Specifically, inappropriate expression of the methyltransferase *METTL3* equipped CAD M $\phi$  to accumulate N<sup>6</sup>-adenosine-modified and stabilized *PVR* mRNA, translating into a CD155<sup>hi</sup> phenotype (Fig. 8). Abnormal CD155 mRNA methylation was already present in M $\phi$  precursor cells and persisted in tissue-infiltrating M $\phi$  populating the atherosclerotic lesion. oxLDL and LPS functioned as potent inducers of *METTL3*, linking the metabolic abnormalities of CAD to epigenetic interference, resulting in impaired antigen-presenting function and T cell hypo-responsiveness. The inability to generate protective immunity against spike protein extended to the EBV glycoprotein 350, identifying the underlying mechanism as a signature in the patients’ immune system. Our data delineate a possible immunotherapy for patients with CAD to strengthen anti-viral immunity and protect these patients from chronic infection, morbidity and mortality.

Besides their role as antigen-presenting cells, M $\phi$  function as critical effector cells in the atherosclerotic plaque where they are the prime cellular partner of tissue-infiltrating T cells<sup>11</sup> and hold a key position as inflammatory amplifiers. The effector portfolio of increased inflammatory potential combined with suppressed antigen-presenting function appears to be specific for CAD M $\phi$ <sup>39</sup>. Specifically, M $\phi$  from patients with CAD differ from those in autoimmune vasculitis by enhanced production of chemokines (CXCL10) and cytokines (IL-6), excluding host inflammation as the underlying cause of M $\phi$  reprogramming. Previous studies have implicated bioenergetic regulation in rendering CAD M $\phi$  pro-inflammatory. Specifically, glucose and pyruvate have been described as drivers of excessive chemokine and cytokine production<sup>39,40</sup>, with mitochondrial ROS inducing post-translational modifications of the glycolytic enzyme PKM2 and nuclear transition of ‘moonlighting’ PKM2 to drive the cytokine hyper-producing state of CAD M $\phi$ <sup>40</sup>. Glucose had no role in turning CAD monocytes and M $\phi$  into *METTL3* and CD155 high expressors, outlining several co-existent metabolic pathways modulating M $\phi$  function in cardiovascular disease.

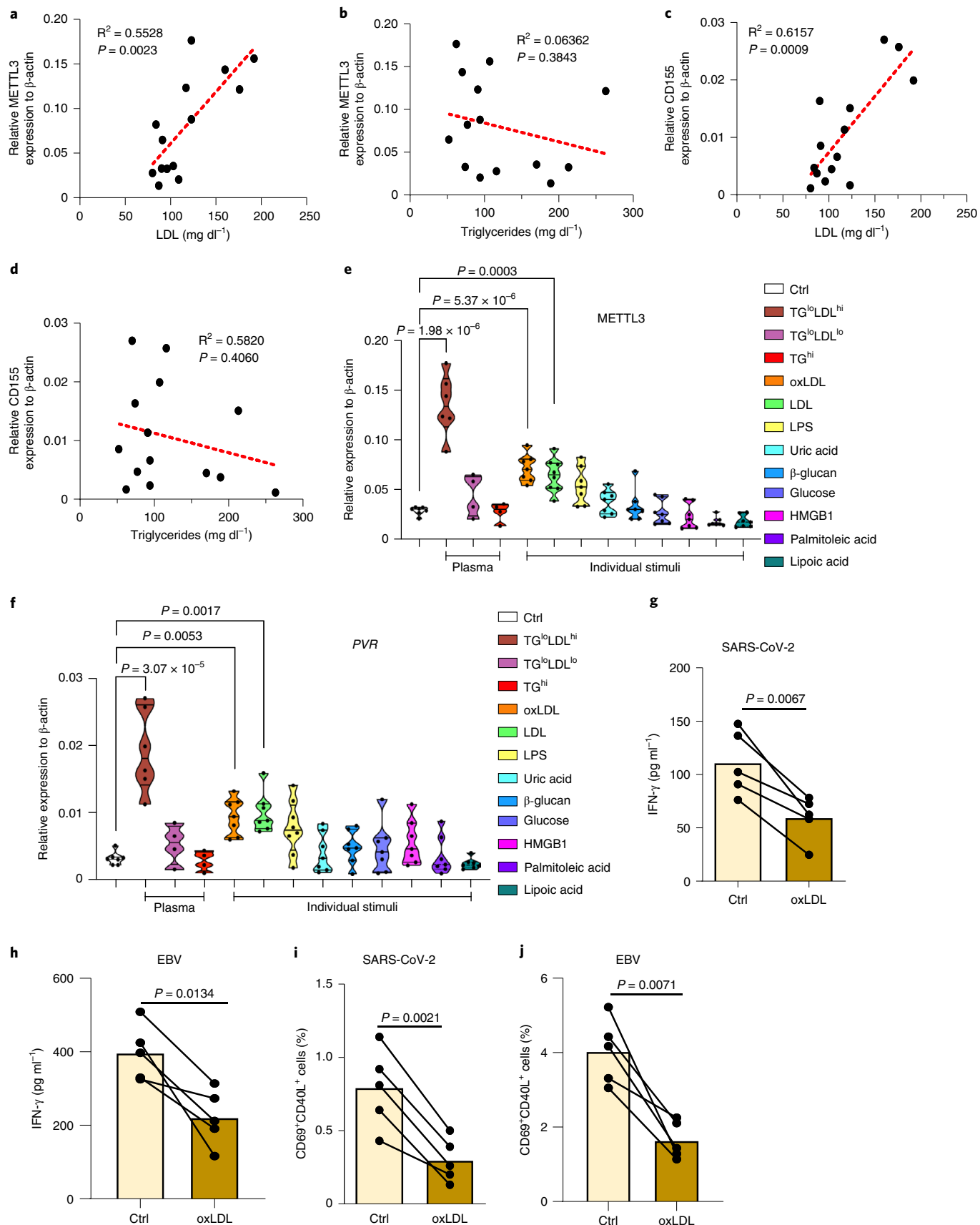
Current data have emphasized the critical position of antigen-presenting M $\phi$  in enabling expansion of spike-protein-reactive and EBV-glycoprotein-350-reactive CD4<sup>+</sup> T cells. Such T cells are a condition sine qua non to render the host immune against SARS-CoV-2 and EBV infection<sup>9,41</sup>. CD4<sup>+</sup> helper T cells are irreplaceable in supporting B cells to produce high-affinity, neutralizing antibodies<sup>42</sup>. Profiling of co-stimulatory and co-inhibitory ligands expressed by CAD M $\phi$  revealed differences exclusively for molecules delivering a negative signal and included both PD-L1 and CD155. PD-L1 is well-established as a regulator of anti-tumor T cells and is successfully targeted in immune checkpoint inhibitor therapy of patients with cancer to unleash anti-tumor immunity<sup>43</sup>. Blockade of CD155 is currently explored as an alternative strategy to enhance T cell responses against tumor antigens<sup>44</sup>. The combined upregulation of PD-L1 and CD155 on CAD M $\phi$  amplifies the immunosuppressive functions of these cells and remains unopposed by co-stimulatory ligands, such as CD80, CD86 and CD40. PD-L1 and CD155 share the effect on anti-viral T cell responses. As previously described for the inhibitory effect of CAD M $\phi$  on the expansion of T cells specific for varicella zoster virus<sup>44</sup>, current data extend the defect in the induction of anti-viral T cells to SARS-CoV-2 and EBV. It is likely that this M $\phi$ -dependent immunodeficiency of patients with CAD has relevance for other antigens, as IFN- $\gamma$  production was effectively suppressed in all immune responses tested. However, upstream signals leading to aberrant PD-L1 and CD155 expression appear to be different. Although the glycolytic breakdown product pyruvate effectively controls upregulation of PD-L1 transcription, *PVR* mRNA was selectively induced by oxLDL and LPS. Thus, both ligands are differentially regulated by the cell’s metabolic microenvironment.

Although the PD-L1<sup>hi</sup> phenotype of CAD M $\phi$  resulted from excess transcriptional activity, higher CD155 expression on the M $\phi$  surface was a consequence of altered mRNA stability. Patient cells accumulated N<sup>6</sup>-methyladenosine (m<sup>6</sup>A)-rich *PVR* mRNA, pointing toward an epitranscriptomic mechanism determining M $\phi$  function. Formation of m<sup>6</sup>A in mRNA is now recognized as a potent

**Fig. 7 | Induction of *PVR* and *METTL3* mRNA expression in monocytes.** a–d. CD14<sup>+</sup> monocytes were isolated from healthy individuals and cultured in human plasma (10%) for 48 hours. Transcripts specific for *METTL3* (a,b) and *PVR* (c,d) were quantified by RT-PCR. Expression levels of *METTL3* and *PVR* mRNA were correlated with LDL (a,c) and TG (b,d) concentrations in 14 different plasma samples. e,f. CD14<sup>+</sup> monocytes were isolated from healthy individuals and primed with the indicated stimuli for 48 hours. *METTL3* and *PVR* mRNA levels were quantified by RT-PCR. Results are given as violin plots. g–j. M $\phi$  from healthy individuals were treated with oxLDL for 2 days and then loaded with antigen and mixed with T cells to measure induction of antigen-specific T cell immunity. IFN- $\gamma$  release in response to SARS-CoV-2 antigen (g) and EBV antigen (h) was quantified in five experiments. Frequencies of SARS-CoV-2-specific CD69<sup>+</sup>CD40L<sup>+</sup>CD4<sup>+</sup> T cells (i) and EBV-specific CD69<sup>+</sup>CD40L<sup>+</sup>CD4<sup>+</sup> T cells (j) were measured in five experiments. Individual data points are displayed. Data are mean  $\pm$  s.e.m. Comparison by one-way ANOVA (e,f) and paired *t*-test (g–j). Correlations analyzed by linear regression. *P* values are shown in each panel.

modification to control gene expression in cellular differentiation and in cancer biology<sup>32</sup>. Remarkably, screening of healthy and CD155<sup>hi</sup> CAD Mφ for m<sup>6</sup>A readers, m<sup>6</sup>A writer complex components

and erasers revealed a selective upregulation of METTL3 in the cells of patients with CAD. METTL3 is the methyltransferase that reversibly modifies mRNA to shape the epitranscriptomic landscape<sup>45</sup> and



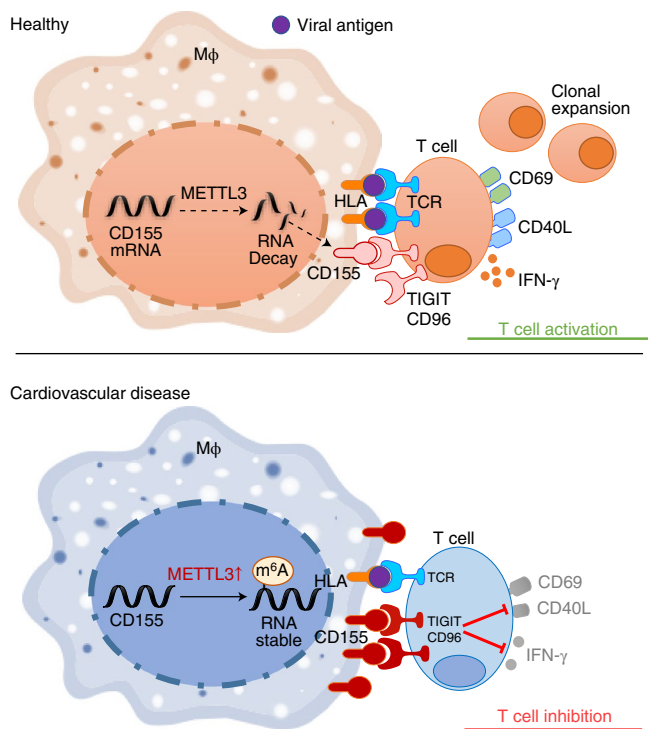


**Fig. 8 | Immunosuppressive macrophages in CAD.** Upper panel: In healthy Mφ, the methyltransferase METTL3 is expressed at a low level; PVR mRNA (encoding for CD155) is relatively unstable, keeping surface expression of CD155 low. Such Mφ present viral antigens to antigen-specific T cells, which differentiate into host-protective memory and effector T cells. Lower panel: High expression of the methyltransferase METTL3 increases m<sup>6</sup>A modifications on CD155 mRNA, which stabilizes the transcripts and results in high surface expression of CD155 protein. CD155 transmits a ‘stop signal’ to T cells that express the CD155 receptors TIGIT or CD96, effectively suppressing anti-viral immunity.

regulates complex processes, such as RNA nuclear export, translation efficiency and polyadenylation<sup>18</sup>. m<sup>6</sup>A modification has been described to play a role in the initiation and progression of human cancers, but there is limited information on the contribution of METTL3 to cellular function of non-malignant cells. The methyltransferase promotes proliferation and fibroblast-to-myofibroblast transition in cardiac remodeling<sup>46</sup> and mediates endothelial activation in response to oscillatory stress<sup>47</sup>. In murine macrophages, METTL3-induced methylation stabilizes *STAT1* mRNA, which serves as a master regulator of M1 polarization, identifying the enzyme as a pro-inflammatory regulator<sup>25</sup>. Opposite to human Mφ, mouse dendritic cells seem to rely on METTL3-mediated mRNA m<sup>6</sup>A methylation for enhanced expression of the co-stimulatory ligands CD40 and CD80, rendering them more effective antigen-presenting cells<sup>26</sup>. Notably, Mφ from patients with CAD responded to changes in their metabolic environment—for example, elevation of oxLDL—to reprogram their functional activities, classifying the high expression of METTL3 as a maladaptive mechanism.

The functional adaptation of Mφ in patients with CAD is best captured by a combination of excess inflammatory activity with a defect in antigen-presenting function. Hybrid Mφ with strong pro-inflammatory capabilities and lacking proficiency in host protection deviate the immune system of patients with CAD, producing inappropriate cytokine release while compromising T cell stimulation. This dilemma has relevance during SARS-CoV-2 infection, known to produce a deleterious cytokine storm while attempting to develop protective immunity. The reprogramming of CAD Mφ

amplifies the negative effects of pro-inflammatory commitment and the lack of appropriate T cell stimulatory capacity. The molecular mechanisms described here offer opportunities to re-educate CAD Mφ to rescue their quintessential contribution to host protection. Reducing exposure of monocytes to oxLDL could provide a preventive measure. More promising would be to directly manipulate the inappropriate activity of METTL3, to reduce the burden of m<sup>6</sup>A modification. Two interventions proved beneficial in enhancing anti-viral T cell reactivity: knockdown of METTL3 and treatment with the m<sup>6</sup>A inhibitor 3-DAA. Improved expansion of anti-viral CD4<sup>+</sup> T cells in vivo is encouraging as such strategies of immune engineering could be translated to the patient. Such mechanism-oriented immune interventions could be valuable during both vaccination and the natural viral infection. Alternatively, blocking access to CD155 or CD96/TIGIT could provide an elegant approach to optimize induction of adaptive immunity and improve the outcome of both vaccination and viral infection in high-risk individuals with pre-existing cardiovascular disease.

## Methods

**Patients.** Patients were defined to have CAD if they had a history of coronary bypass surgery, history of coronary stent placement or documented myocardial infarction. To eliminate inflammatory activity directly related to myocardial ischemia, 87 patients were enrolled who were at least 90 days post-event. Detailed clinical features of enrolled patients are displayed in Extended Data Table 1. Healthy controls had no evidence for CAD based on evaluation by a physician. Recruitment criteria included no personal history of cancer, chemotherapy, chronic inflammatory disease, chronic viral infection or autoimmune disease. Because the patient samples were collected early during the COVID-19 pandemic, only one study participant had recorded COVID-19 infection before testing. In total, 93.75% of study participants carried antibodies against EBV nuclear antigen (EBNA). The institutional review boards at Stanford University and at Mayo Clinic reviewed and approved the study protocol. All participants were informed appropriately, and written consent documents based on the Declaration of Helsinki were signed by all participants.

**Cell culture.** PBMCs were purified by density gradient centrifugation with Lymphoprep (STEMCELL Technologies), as previously described<sup>40</sup>. Memory CD4<sup>+</sup> T cells were isolated by negative selection with EasySep human cell isolation kits (STEMCELL Technologies, 19157). Monocytes were isolated as previously reported<sup>14</sup>. To induce macrophages, monocytes were treated with 20 ng ml<sup>-1</sup> of M-CSF (BioLegend) for 5 days in 10% FBS (Lonza) and were differentiated by stimulation with 100 ng ml<sup>-1</sup> of LPS (Sigma-Aldrich) and 100 U ml<sup>-1</sup> of IFN-γ (Sino Biological) for 24 hours. Mφ were detached from the culture plates with Accutase Cell Detachment Solution (Innovative Cell Technologies) for 10 minutes at 37°C. CD155 and METTL3 knockdown was performed with Lipofectamine 3000 transfection reagent (Thermo Fisher Scientific) using corresponding 10 nM siRNA (Santa Cruz Biotechnology).

**In vitro antigen presentation assay.** PBMCs (2 × 10<sup>6</sup>) were primed with viral antigens (1 μg ml<sup>-1</sup> of SARS-CoV-2 spike protein, 1 μg ml<sup>-1</sup> of SARS-CoV-2 nucleocapsid protein and 1 μg ml<sup>-1</sup> of EBV glycoprotein gp350) in RPMI 1640 medium supplemented with 10% FBS for 5 days. For recall responses, antigen-stimulated PBMCs were washed on day 5 and kept in antigen-free medium for 24 hours to remove the antigens. On day 6, primed PBMCs were mixed with syngeneic macrophages (2 × 10<sup>5</sup>) that had been loaded with antigen by overnight culture. Six hours later, T cell activation was measured by flow cytometry staining for the surface receptors CD69 and CD40L. IFN-γ production in the supernatant was quantified with the IFN-γ High Sensitivity Human ELISA Kit assay system (Abcam). Supernatants were collected after 24 hours of antigen rechallenge. Naive and memory CD4<sup>+</sup> T cells were isolated by negative selection with EasySep Human Naive CD4<sup>+</sup> T Cell Isolation Kit II (STEMCELL Technologies, 17555) and EasySep Human Memory CD4<sup>+</sup> T Cell Enrichment Kit (STEMCELL Technologies, 19157), respectively.

**Monocyte priming.** CD14<sup>+</sup> monocytes were isolated from PBMCs of healthy individuals with EasySep Human Monocyte Isolation Kit (STEMCELL Technologies, 19359). Monocytes were cultured in medium supplemented with 10% plasma from human donors with known concentrations of TGs, LDL and HDL. Detailed lipid profiles are shown in Extended Data Table 2. Plasma samples were categorized in TG-high; TG-low plus LDL-low; and TG-low plus LDL-high. In parallel, monocytes were treated with oxLDL (50 μg ml<sup>-1</sup>), LDL (100 μg ml<sup>-1</sup>), uric acid (10 mM), β-glucan (1 μM), glucose (50 mM), HMGB-1 (100 ng ml<sup>-1</sup>), palmitic acid (0.5 mM) and lipoic acid (1 mM), respectively. After 48 hours, *METTL3* and *PVR* mRNAs were quantified by RT-PCR.

**Flow cytometry.** Cell surface staining was performed as previously described<sup>48</sup>. Data were collected using a BD LSRFortessa flow cytometer or a CYTEK NL-3000 and analyzed by FlowJo 10.0 (Tree Star). The following antibodies were used for staining: Brilliant Violet 785 anti-human CD154 antibody (BioLegend, 310842, 1:100), Brilliant Violet 510 anti-human CD69 antibody (BioLegend, 310936, 1:100), Brilliant Violet 421 anti-human CD3 antibody (BioLegend, 344834, 1:100), PE/Cyanine7 anti-human CD4 antibody (BioLegend, 34357410, 1:100), Brilliant Violet 650 anti-human CD8 antibody (BioLegend, 344730, 1:100), APC/Cyanine7 anti-human CD45RA antibody (BioLegend, 304128, 1:100), FITC anti-human CD45RO antibody (BioLegend, 304242, 1:100), PerCP/Cyanine5.5 anti-human CD38 antibody (BioLegend, 356614, 1:100), Brilliant Violet 711 anti-human CD163 antibody (BioLegend, 333630, 1:100), PE/Cyanine7 anti-human CD45 antibody (BioLegend, 368532, 1:100), Brilliant Violet 711 anti-human CD4 antibody (BioLegend, 317439, 1:100), Pacific Blue anti-human HLA-DR antibody (BioLegend, 307624, 1:100), APC anti-human CD206 (MMR) antibody (BioLegend, 321110, 1:100) and PE anti-human CD155 (PVR) antibody (BioLegend, 337610, 1:100). Detailed information of all antibodies used is listed in Supplementary Table 2.

**RNA extraction and RT-PCR.** Direct-zol RNA MiniPrep kits were supplied by Genesee Scientific to extract total RNA from the samples. Reverse transcription was performed with High-Capacity cDNA Reverse Transcription Kits (Thermo Fisher Scientific). SYBR Green qPCR Master Mix (Bimake) was used for quantitative RT-PCR. Samples were analyzed with a RealPlex2 Mastercycler (Eppendorf). Gene relative expression levels were normalized to the expression of  $\beta$ -actin transcripts. Primers for RT-PCR are listed in Supplementary Table 3.

**Immunofluorescence and confocal microscopy.** The methods used for dual-color immunostaining were previously described<sup>49</sup>. Cells were fixed with 4% paraformaldehyde solution (Affymetrix) in glass-bottom tissue culture plates and incubated with primary antibody at 4 °C overnight, followed by fluorescence-conjugated secondary antibody at room temperature for 2 hours. For tissue staining, atherosclerotic plaques were cut into 4- $\mu$ m-thick sections and permeabilized with 0.5% Triton X-100 in PBS for 20 minutes. Tissue sections were incubated with primary antibodies for overnight at 4 °C and secondary antibodies for 1 hour at 37 °C. Nuclei were labeled with DAPI (Santa Cruz Biotechnology) for 10 minutes at room temperature. Images were analyzed using the Olympus fluorescence microscopy system or the All-in-One Fluorescence Microscope BZX800E system (Keyence). The following antibodies were used: CD155 monoclonal antibody (Thermo Fisher Scientific, MA5-13493, 1:200), CD68 monoclonal antibody (Thermo Fisher Scientific, MA5-13324, 1:200), METTL3 (E3F2A) rabbit monoclonal antibody (Cell Signaling Technology, 86132S, 1:200), goat anti-rabbit IgG (H+L) Alexa Fluor 488 (Thermo Fisher Scientific, A-11008, 1:200) and goat anti-mouse IgG (H+L) Alexa Fluor 594 (Thermo Fisher Scientific, A-31635, 1:200). Detailed information of all antibodies used is listed in Supplementary Table 2.

**Western blotting.** Techniques applied for immunoblotting were previously reported<sup>49</sup>. Basically, cells were harvested and lysed with RIPA buffer (Abcam) supplemented with proteinase inhibitor (Thermo Fisher Scientific). Proteins were electrophoresed in 4–15% SDS-PAGE (Bio-Rad, 4561083) and transferred to PVDF membranes (Bio-Rad, 1620177). After 1-hour blocking in 2% BSA, membranes were incubated with primary antibody anti-METTL3 (E3F2A) rabbit monoclonal antibody (Cell Signaling Technology, 86132S, 1:500) at 4 °C for overnight and secondary antibody anti-rabbit IgG HRP-linked antibody (Cell Signaling Technology 7074S, 1:10,000) at room temperature for 1 hour. Antibody binding was detected by SuperSignal West Femto Maximum Sensitivity Substrate (Thermo Fisher Scientific, 34094).

**RNA decay assays.** To measure RNA stability, the transcription inhibitor actinomycin D was added to the culture at the dose of 10  $\mu$ g ml<sup>-1</sup>. Samples were harvested at 0-, 2-, 4- and 8-hour timepoints. RNA and cDNA were prepared as described above, and remaining transcripts were quantified with qRT-PCR.

**Me-RIP.** Me-RIP assays were performed using the EpiQuik CUT&RUN m6A RNA Enrichment Kit (EpiGentek, P-9018). In brief, 10  $\mu$ g of total RNA was incubated with a beads-bound m6A capture antibody and isotype IgG antibody, respectively, for 90 minutes at room temperature. The enriched RNA fragments were released and purified with RNA binding beads. Eluted mRNA was reverse transcribed into cDNA and quantified with qRT-PCR.

**In vivo antigen presentation assay.** NSG mice were obtained from The Jackson Laboratory and maintained in specific pathogen-free conditions at 20–22 °C and on a 12-hour light/dark cycle. All mice had free access to water and food. NSG mice were immuno-reconstituted by adoptive transfer of  $1 \times 10^7$  PBMCs as previously described<sup>50,51</sup>. Syngeneic monocytes were differentiated into M $\phi$  ( $1 \times 10^6$ ) and loaded with SARS-CoV-2 protein (1  $\mu$ g ml<sup>-1</sup>) for 24 hours before injection into the mice. Reconstituted mice were primed with SARS-CoV-2 protein (10  $\mu$ g) or vehicle intraperitoneally. After 7 days, the spleen was harvested, and activated human

T cells were evaluated by surface staining with fluorescence-conjugated anti-human CD45, CD3, CD4 and CD38 antibodies. All experiments were approved and performed in accordance with the guidelines of the Institutional Animal Care and Use Committee.

**Cell survival quantification.** Three different approaches were used to measure the survival of M $\phi$ <sup>50</sup>. Live/dead staining was performed with the LIVE/DEAD Cell Imaging Kit (488/570) (Thermo Fisher Scientific). The release of lactate dehydrogenase (LDH) by dead cells was evaluated with the Pierce LDH Cytotoxicity Assay (Thermo Fisher Scientific) in the culture supernatant of M $\phi$ . Relative cell viability was quantified with the alamarBlue Cell Viability Reagent (Thermo Fisher Scientific). All assays were performed following the manufacturers' instructions.

**Prediction of m6A DRACH sites.** The full-length PVR cDNA sequence was analyzed with the open-access m6A prediction server SRAMP<sup>34</sup>, and 12 DRACH motifs with high confidentiality score were identified. By analyzing a Me-RIP database from the human myeloid cell lines monomac-6 (GSE76414)<sup>35</sup> and nomo-1 (GSE87190)<sup>36</sup>, ten m6A peaks were found; most peaks were localized in two regions of the 3' UTR of PVR mRNA. We then mapped the predicted sites and peaks back to PVR mRNA, yielding six potential DRACH sites.

**RT-PCR-based quantification of m6A.** For site-specific detection and quantification of m6A sites, we applied a RT-PCR-based approach<sup>37</sup>. Retro-transcription of CD155 was performed with two different enzymes, BstI and MRT, using primers including (RT<sup>+</sup>) and excluding (RT<sup>-</sup>) the m6A sites. m6A modification diminishes the retro-transcription capability of BstI enzyme but not MRT enzyme. Differences in retro-transcription between the two enzymes were detected with qPCR and agarose gel electrophoresis. The primer sequences are listed in Supplementary Table 4.

**Luciferase reporter assay.** The 3' UTRs of CD155 with or without mutated m6A sites were cloned downstream of the firefly luciferase translation sequence of the pMIR-REPORT vector (Thermo Fisher Scientific). Activation of the luciferase reporter reflects to which degree changes in the 3' UTR regulate gene transcription. Recombinant plasmids were transfected into control or CAD M $\phi$  with Lipofectamine 3000 transfection reagent. A control Renilla luciferase plasmid was used to normalize the transfection efficiency. Luciferase activities were tested with the Dual-Luciferase Reporter Assay System (Promega). Relative luciferase activity was calculated by dividing the firefly luminescence by the Renilla luminescence.

**Statistics.** All data analyses applied GraphPad Prism 8.0 (GraphPad Software). Normal distribution of all datasets was confirmed. All data are shown as mean  $\pm$  s.e.m., and values of  $P < 0.05$  were considered statistically significant. Two-tailed Student's *t*-test and paired one-way ANOVA were applied to compare groups. Two-way ANOVA with Bonferroni's post test was used to compare data collected over time.

**Reporting summary.** Further information on research design is available in the Nature Research Reporting Summary linked to this article.

## Data availability

All data generated or analyzed are included in the main article and associated files. Source data are provided with this paper. Potential m6A DRACH sites were predicted with publically available data at GSE76414 and GSE87190.

Received: 13 December 2021; Accepted: 7 June 2022;

Published online: 13 July 2022

## References

- Clerkin, K. J. et al. COVID-19 and cardiovascular disease. *Circulation* **141**, 1648–1655 (2020).
- Madjid, M. et al. Influenza epidemics and acute respiratory disease activity are associated with a surge in autopsy-confirmed coronary heart disease death: results from 8 years of autopsies in 34,892 subjects. *Eur. Heart J.* **28**, 1205–1210 (2007).
- Macias, A. E. et al. The disease burden of influenza beyond respiratory illness. *Vaccine* **39**, A6–A14 (2021).
- Joesoef, R. M., Harpaz, R., Leung, J. & Bialek, S. R. Chronic medical conditions as risk factors for herpes zoster. *Mayo Clin. Proc.* **87**, 961–967 (2012).
- Offor, U. T. et al. Transplantation for congenital heart disease is associated with an increased risk of Epstein–Barr virus-related post-transplant lymphoproliferative disorder in children. *J. Heart Lung Transplant.* **40**, 24–32 (2021).
- Onishi, Y. et al. Resolution of chronic active EBV infection and coexisting pulmonary arterial hypertension after cord blood transplantation. *Bone Marrow Transplant.* **49**, 1343–1344 (2014).

7. Sette, A. & Crotty, S. Adaptive immunity to SARS-CoV-2 and COVID-19. *Cell* **184**, 861–880 (2021).
8. Grifoni, A. et al. Targets of T cell responses to SARS-CoV-2 coronavirus in humans with COVID-19 disease and unexposed individuals. *Cell* **181**, 1489–1501 (2020).
9. Dan, J. M. et al. Immunological memory to SARS-CoV-2 assessed for up to 8 months after infection. *Science* **371**, eabf4063 (2021).
10. Amyes, E. et al. Characterization of the CD4<sup>+</sup> T cell response to Epstein–Barr virus during primary and persistent infection. *J. Exp. Med.* **198**, 903–911 (2003).
11. Fernandez, D. M. et al. Single-cell immune landscape of human atherosclerotic plaques. *Nat. Med.* **25**, 1576–1588 (2019).
12. Flego, D., Liuzzo, G., Weyand, C. M. & Crea, F. Adaptive immunity dysregulation in acute coronary syndromes: from cellular and molecular basis to clinical implications. *J. Am. Coll. Cardiol.* **68**, 2107–2117 (2016).
13. Nakajima, T. et al. De novo expression of killer immunoglobulin-like receptors and signaling proteins regulates the cytotoxic function of CD4 T cells in acute coronary syndromes. *Circ. Res.* **93**, 106–113 (2003).
14. Watanabe, R. et al. Pyruvate controls the checkpoint inhibitor PD-L1 and suppresses T cell immunity. *J. Clin. Invest.* **127**, 2725–2738 (2017).
15. Lupo, K. B. & Matosevic, S. CD155 immunoregulation as a target for natural killer cell immunotherapy in glioblastoma. *J. Hematol. Oncol.* **13**, 76 (2020).
16. Yu, X. et al. The surface protein TIGIT suppresses T cell activation by promoting the generation of mature immunoregulatory dendritic cells. *Nat. Immunol.* **10**, 48–57 (2009).
17. Freed-Pastor, W. A. et al. The CD155/TIGIT axis promotes and maintains immune evasion in neoantigen-expressing pancreatic cancer. *Cancer Cell* **39**, 1342–1360 (2021).
18. Frye, M., Harada, B. T., Behm, M. & He, C. RNA modifications modulate gene expression during development. *Science* **361**, 1346–1349 (2018).
19. Dominissini, D. et al. Topology of the human and mouse m<sup>6</sup>A RNA methylomes revealed by m<sup>6</sup>A-seq. *Nature* **485**, 201–206 (2012).
20. Fu, Y., Dominissini, D., Rechavi, G. & He, C. Gene expression regulation mediated through reversible m<sup>6</sup>A RNA methylation. *Nat. Rev. Genet.* **15**, 293–306 (2014).
21. Roundtree, I. A., Evans, M. E., Pan, T. & He, C. Dynamic RNA modifications in gene expression regulation. *Cell* **169**, 1187–1200 (2017).
22. Geula, S. et al. m<sup>6</sup>A mRNA methylation facilitates resolution of naive pluripotency toward differentiation. *Science* **347**, 1002–1006 (2015).
23. Lin, S., Choe, J., Du, P., Triboulet, R. & Gregory, R. I. The m<sup>6</sup>A methyltransferase METTL3 promotes translation in human cancer cells. *Mol. Cell* **62**, 335–345 (2016).
24. Dorn, L. E. et al. The N<sup>6</sup>-methyladenosine mRNA methylase METTL3 controls cardiac homeostasis and hypertrophy. *Circulation* **139**, 533–545 (2019).
25. Liu, Y. et al. The N<sup>6</sup>-methyladenosine (m<sup>6</sup>A)-forming enzyme METTL3 facilitates M1 macrophage polarization through the methylation of STAT1 mRNA. *Am. J. Physiol. Cell Physiol.* **317**, C762–C775 (2019).
26. Wang, H. et al. Mettl3-mediated mRNA m(6)A methylation promotes dendritic cell activation. *Nat. Commun.* **10**, 1898 (2019).
27. Meckiff, B. J. et al. Imbalance of regulatory and cytotoxic SARS-CoV-2-reactive CD4<sup>+</sup> T cells in COVID-19. *Cell* **183**, 1340–1353 (2020).
28. Sahin, U. et al. COVID-19 vaccine BNT162b1 elicits human antibody and TH1 T cell responses. *Nature* **586**, 594–599 (2020).
29. Jackson, L. A. et al. An mRNA vaccine against SARS-CoV-2—preliminary report. *N. Engl. J. Med.* **383**, 1920–1931 (2020).
30. Chen, L. & Flies, D. B. Molecular mechanisms of T cell co-stimulation and co-inhibition. *Nat. Rev. Immunol.* **13**, 227–242 (2013).
31. Lugowski, A., Nicholson, B. & Rissland, O. S. Determining mRNA half-lives on a transcriptome-wide scale. *Methods* **137**, 90–98 (2018).
32. Zaccara, S., Ries, R. J. & Jaffrey, S. R. Reading, writing and erasing mRNA methylation. *Nat. Rev. Mol. Cell Biol.* **20**, 608–624 (2019).
33. Chang, Y. et al. Single-cell transcriptomic identified HIF1A as a target for attenuating acute rejection after heart transplantation. *Basic Res. Cardiol.* **116**, 64 (2021).
34. Zhou, Y., Zeng, P., Li, Y. H., Zhang, Z. & Cui, Q. SRAMP: prediction of mammalian N<sup>6</sup>-methyladenosine (m<sup>6</sup>A) sites based on sequence-derived features. *Nucleic Acids Res.* **44**, e91 (2016).
35. Li, Z. et al. FTO plays an oncogenic role in acute myeloid leukemia as a N<sup>6</sup>-methyladenosine RNA demethylase. *Cancer Cell* **31**, 127–141 (2017).
36. Su, R. et al. R-2HG exhibits anti-tumor activity by targeting FTO/m<sup>6</sup>A/MYC/CEBPA signaling. *Cell* **172**, 90–105 (2018).
37. Olazagoitia-Garmendia, A. & Castellanos-Rubio, A. Relative quantification of residue-specific m<sup>6</sup>A RNA methylation using m<sup>6</sup>A-RT-QPCR. *Methods Mol. Biol.* **2298**, 185–195 (2021).
38. Netea, M. G. et al. Trained immunity: a program of innate immune memory in health and disease. *Science* **352**, aaf1098 (2016).
39. Watanabe, R. et al. Glucose metabolism controls disease-specific signatures of macrophage effector functions. *JCI Insight* **3**, e123047 (2018).
40. Shirai, T. et al. The glycolytic enzyme PKM2 bridges metabolic and inflammatory dysfunction in coronary artery disease. *J. Exp. Med.* **213**, 337–354 (2016).
41. Jung, S. et al. DNA-mediated immunization of glycoprotein 350 of Epstein–Barr virus induces the effective humoral and cellular immune responses against the antigen. *Mol. Cells* **12**, 41–49 (2001).
42. Luckheeram, R. V., Zhou, R., Verma, A. D. & Xia, B. CD4<sup>+</sup> T cells: differentiation and functions. *Clin. Dev. Immunol.* **2012**, 925135 (2012).
43. Daassi, D., Mahoney, K. M. & Freeman, G. J. The importance of exosomal PDL1 in tumour immune evasion. *Nat. Rev. Immunol.* **20**, 209–215 (2020).
44. O'Donnell, J. S., Madore, J., Li, X. Y. & Smyth, M. J. Tumor intrinsic and extrinsic immune functions of CD155. *Semin. Cancer Biol.* **65**, 189–196 (2020).
45. Shi, H., Wei, J. & He, C. Where, when, and how: context-dependent functions of RNA methylation writers, readers, and erasers. *Mol. Cell* **74**, 640–650 (2019).
46. Li, T. et al. Silencing of METTL3 attenuates cardiac fibrosis induced by myocardial infarction via inhibiting the activation of cardiac fibroblasts. *FASEB J.* **35**, e21162 (2021).
47. Chien, C. S. et al. METTL3-dependent N<sup>6</sup>-methyladenosine RNA modification mediates the atherogenic inflammatory cascades in vascular endothelium. *Proc. Natl. Acad. Sci. USA* **118**, e2025070118 (2021).
48. Jin, K. et al. NOTCH-induced rerouting of endosomal trafficking disables regulatory T cells in vasculitis. *J. Clin. Invest.* **131**, e136042 (2021).
49. Wen, Z. et al. N-myristoyltransferase deficiency impairs activation of kinase AMPK and promotes synovial tissue inflammation. *Nat. Immunol.* **20**, 313–325 (2019).
50. Li, Y. et al. The DNA repair nuclease MRE11A functions as a mitochondrial protector and prevents T cell pyroptosis and tissue inflammation. *Cell Metab* **30**, 477–492 (2019).
51. Wen, Z. et al. The microvascular niche instructs T cells in large vessel vasculitis via the VEGF-Jagged1-Notch pathway. *Sci. Transl. Med.* **9**, eaal3322 (2017).

## Acknowledgements

This work was supported by the National Institutes of Health (R01AR042527, R01AI108906, R01HL142068 and P01HL129941 to C.M.W. and R01AI108891, R01AG045779, U19AI057266 and R01AI129191 to J.J.G.) and the Encrantz Family Discovery Fund.

## Author contributions

Conceptualization: C.M.W. and J.J.G.; Formal analysis: T.V.Z. and Z.H.; Investigation: T.V.Z., Z.H., S.O., K.J., B.W. and G.J.B.; Patient recruitment: R.L.F. and G.J.B.; Writing—original draft: C.M.W., J.J.G. and T.V.Z.; Supervision: C.M.W., J.J.G. and G.J.B.; Funding acquisition: C.M.W. and J.J.G.

## Competing interests

The authors declare no conflicts of interest.

## Additional information

**Supplementary information** The online version contains supplementary material available at <https://doi.org/10.1038/s44161-022-00096-8>.

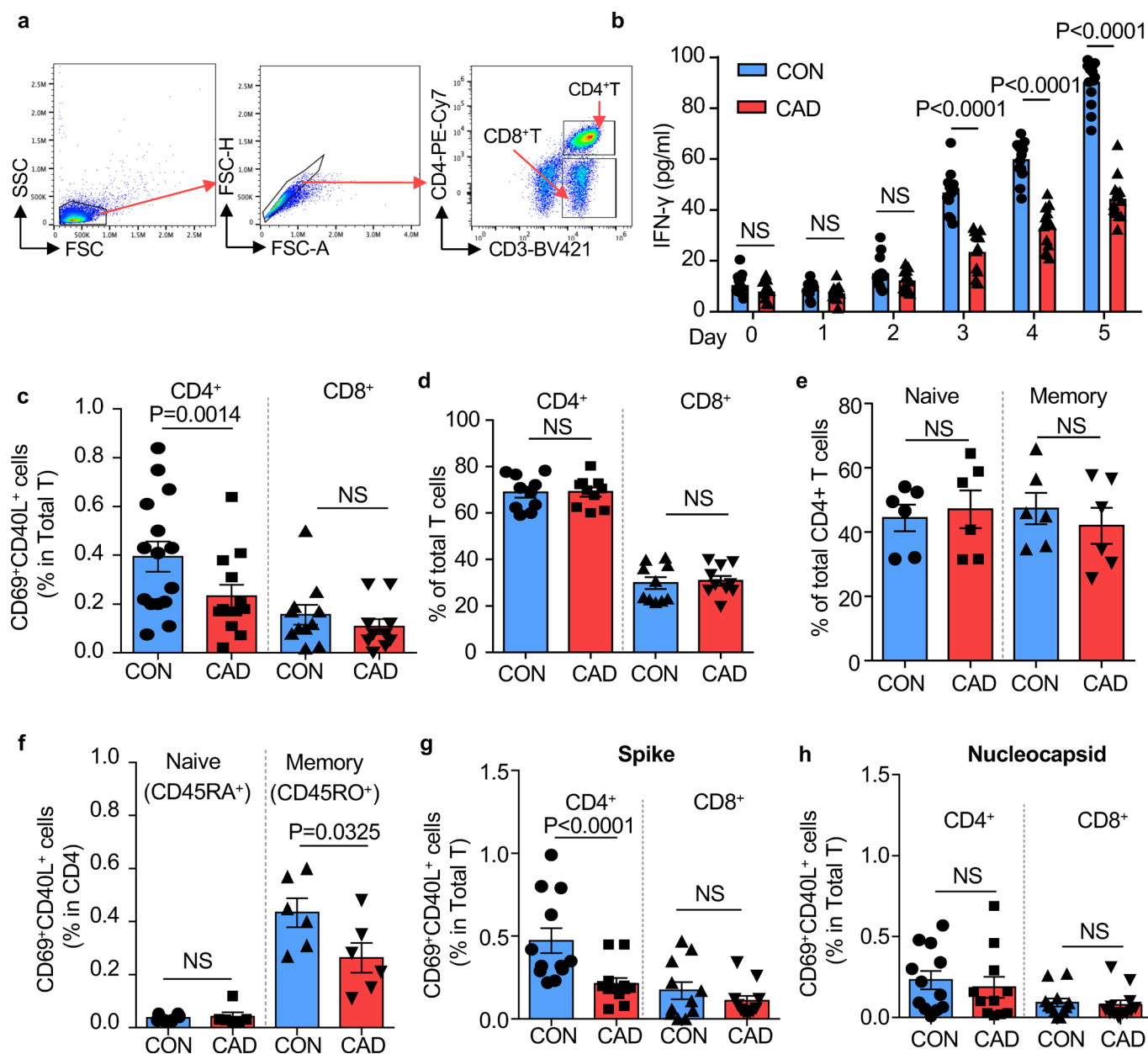
**Correspondence and requests for materials** should be addressed to Cornelia M. Weyand.

**Peer review information** *Nature Cardiovascular Research* thanks Siroon Bekkering and the other, anonymous, reviewer(s) for their contribution to the peer review of this work.

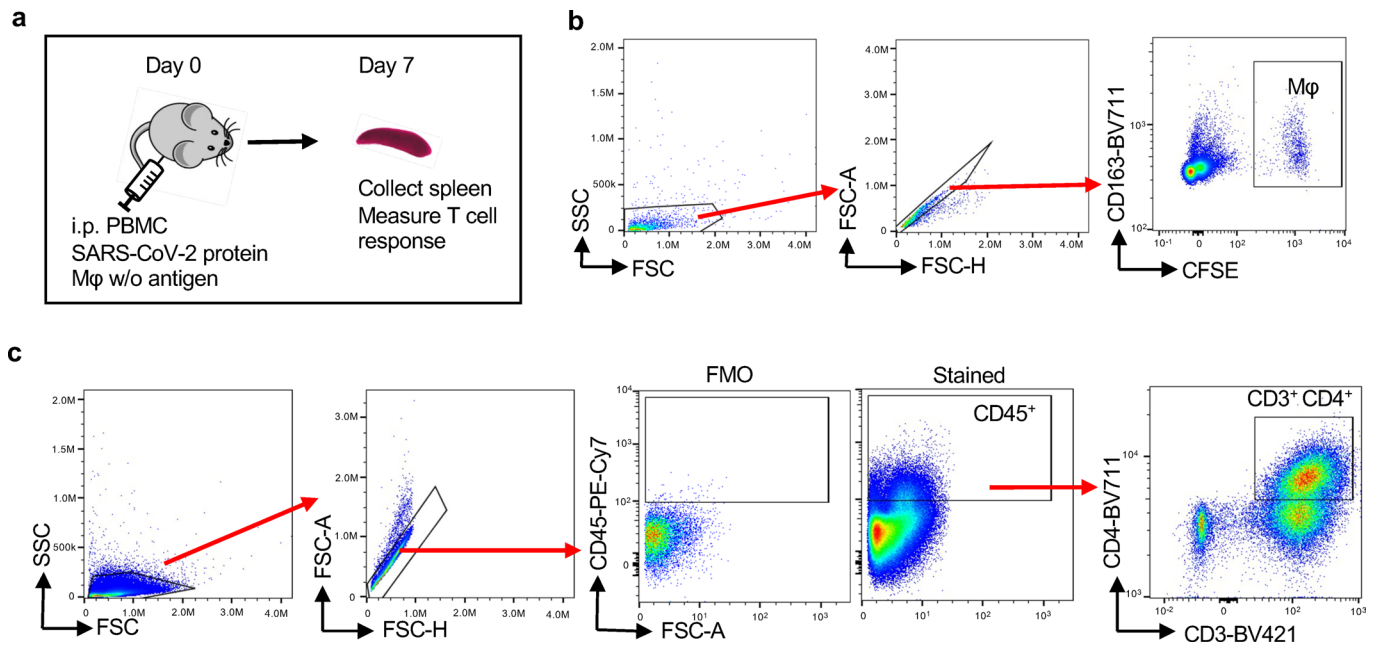
**Reprints and permissions information** is available at [www.nature.com/reprints](http://www.nature.com/reprints).

**Publisher's note** Springer Nature remains neutral with regard to jurisdictional claims in published maps and institutional affiliations.

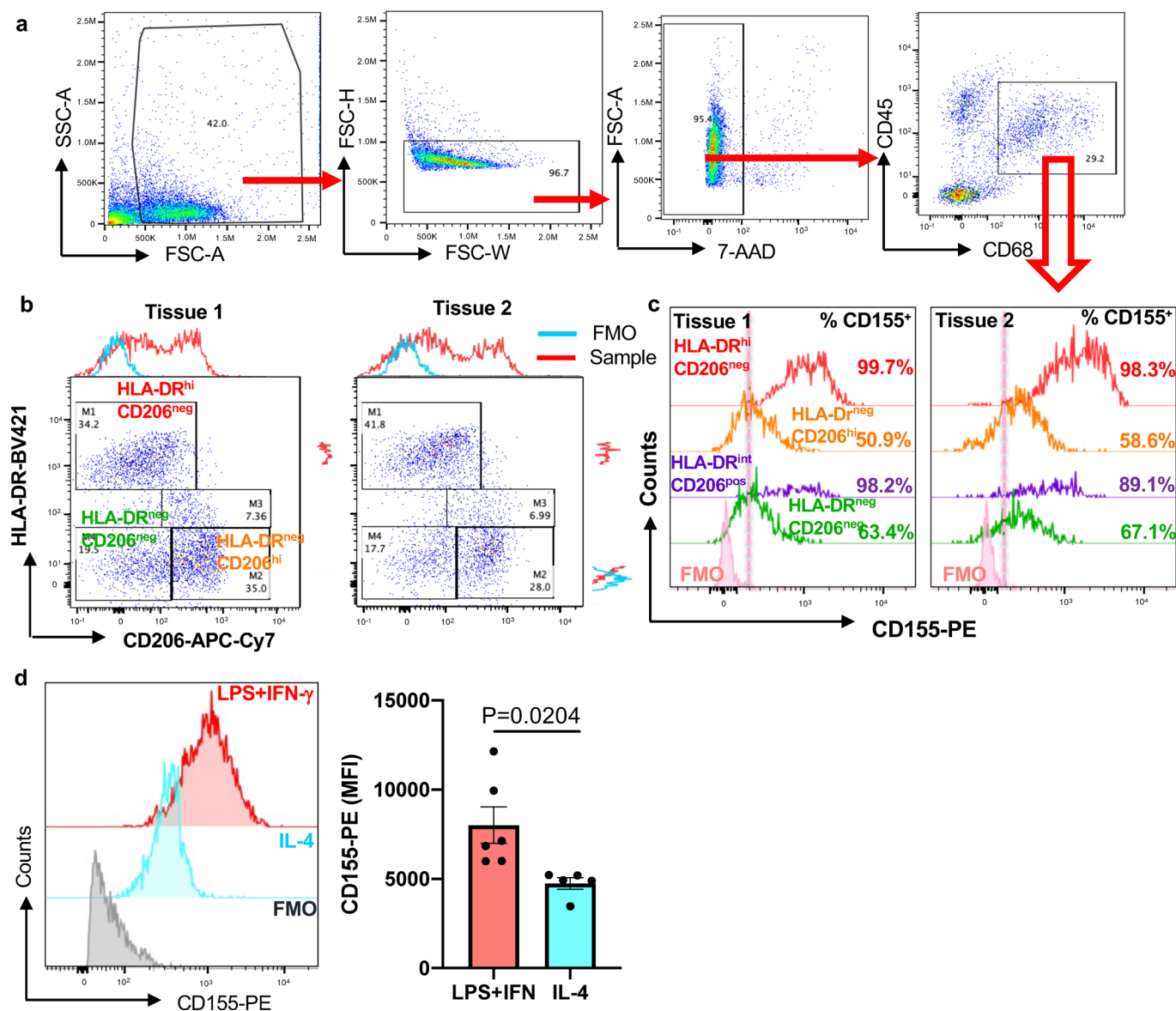
© The Author(s), under exclusive licence to Springer Nature Limited 2022



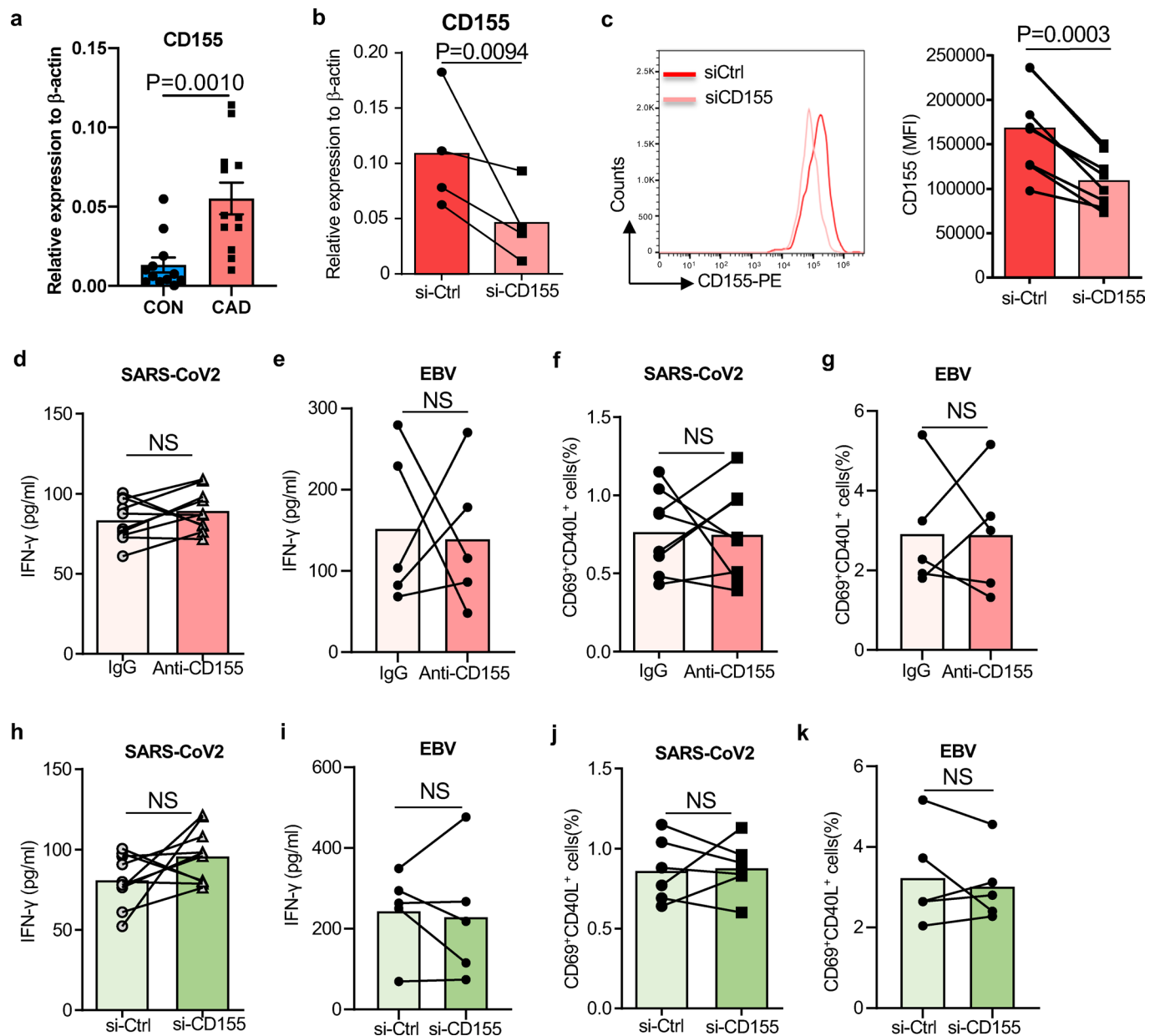
**Extended Data Fig. 1 | Blunted anti-viral T cell responses in patients with coronary artery disease (CAD).** PBMCs were harvested from coronary artery disease (CAD) patients and healthy controls (CON) and stimulated with a mixture of SARS-CoV2 spike and nucleocapsid proteins (1 μg/ml) for 5 days. **a.** Gating strategy to detect T cell subpopulations. Cells in the CD4<sup>+</sup>T gate correspond to data in Figs. 1c,e,g,i,2h,j,l,m,6d,e,h,i,7i and j. **b.** IFN-γ production by antigen-stimulated T cells in patients and controls measured over a period of 5 days. n = 14. **c.** Frequencies of antigen-reactive T cells in the CD4<sup>+</sup> and CD8<sup>+</sup> subpopulations. Data from 14 controls and 12 patients. **d.** Comparison of CD4<sup>+</sup> and CD8<sup>+</sup> T cell frequencies in patients and controls. n = 10. **e.** Frequencies of naïve CD45RA<sup>+</sup> and memory CD45RO<sup>+</sup> T cells amongst control and patient-derived CD4<sup>+</sup> T cells. n = 6. **f.** Frequencies of antigen-reactive CD4<sup>+</sup> T cells within the naïve (CD45RA<sup>+</sup>) and memory (CD45RO<sup>+</sup>) population. n = 6. **g.-h.** T cells were stimulated with SARS-CoV2 spike (**g**) or nucleocapsid (**h**) protein. Percentages of CD4<sup>+</sup> CD69<sup>+</sup> CD40L<sup>+</sup> and CD8<sup>+</sup> CD69<sup>+</sup> CD40L<sup>+</sup> T cells were measured by flow cytometry. n = 12 for spike, n = 10 for nucleocapsid. Individual data points are displayed. Data are mean ± SEM. Differences were compared with one-way ANOVA. p-value was shown on each panel.



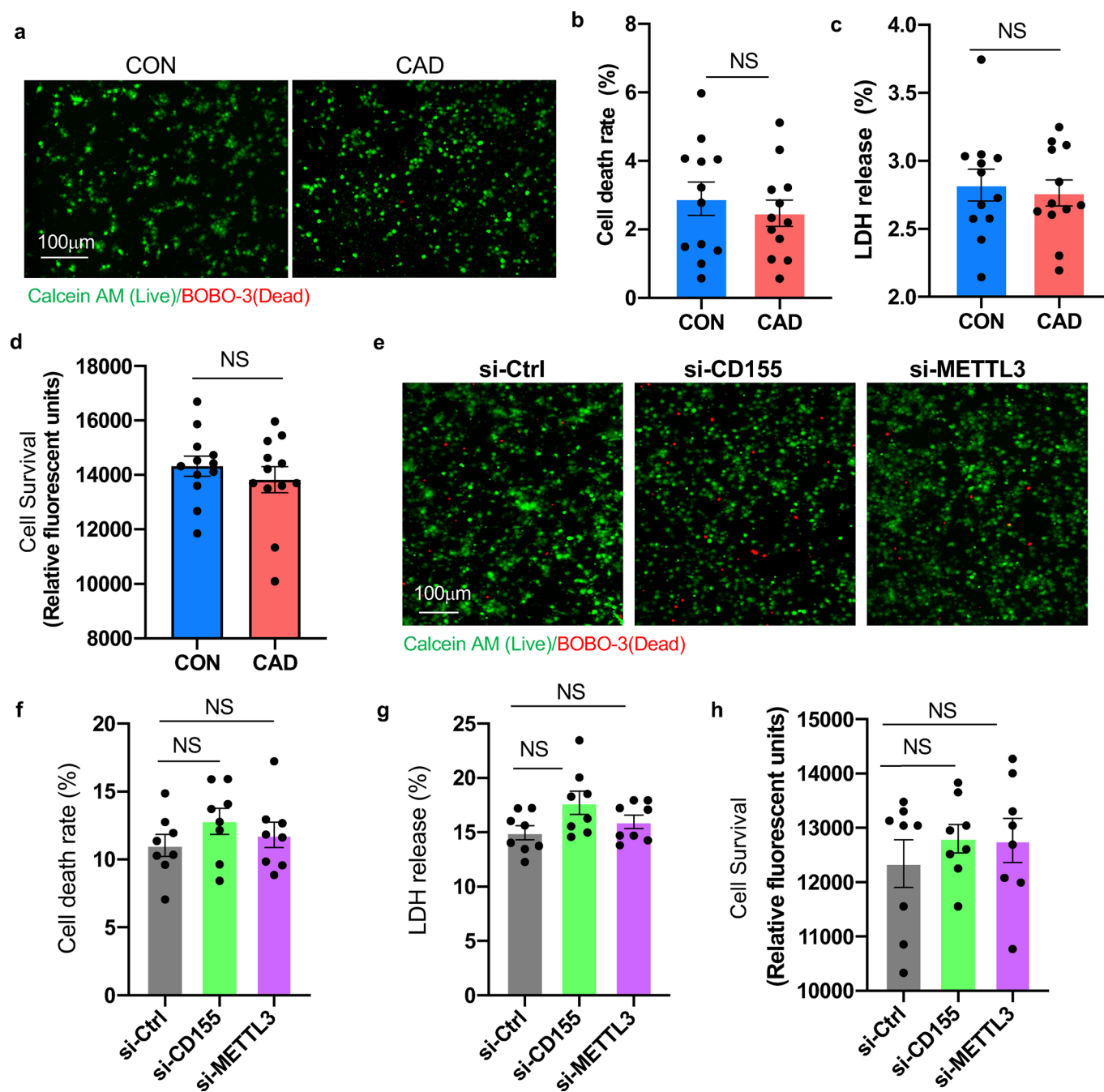
**Extended Data Fig. 2 | In vivo testing of antigen-reactive T cells.** NSG mice were immuno-reconstituted with human PBMC (10 million/mouse) and immunized with SARS-CoV-2 protein (10  $\mu$ g/mouse). In addition, mice received CFSE-labeled autologous Mφ loaded with SARS-CoV-2 protein. After 7 days, the spleen was harvested and activation markers on human CD3<sup>+</sup> CD4<sup>+</sup> T cells were analyzed by flow cytometry. **a.** Schematic graph for the in vivo model. **b.** Flow cytometric detection of CFSE<sup>+</sup> CD163<sup>+</sup> human macrophages in the spleen. **c.** Gating strategy for human T cells in the spleen. Cells in CD3<sup>+</sup>CD4<sup>+</sup> gate were correspond with Figs. 1j, 2n and 6j.



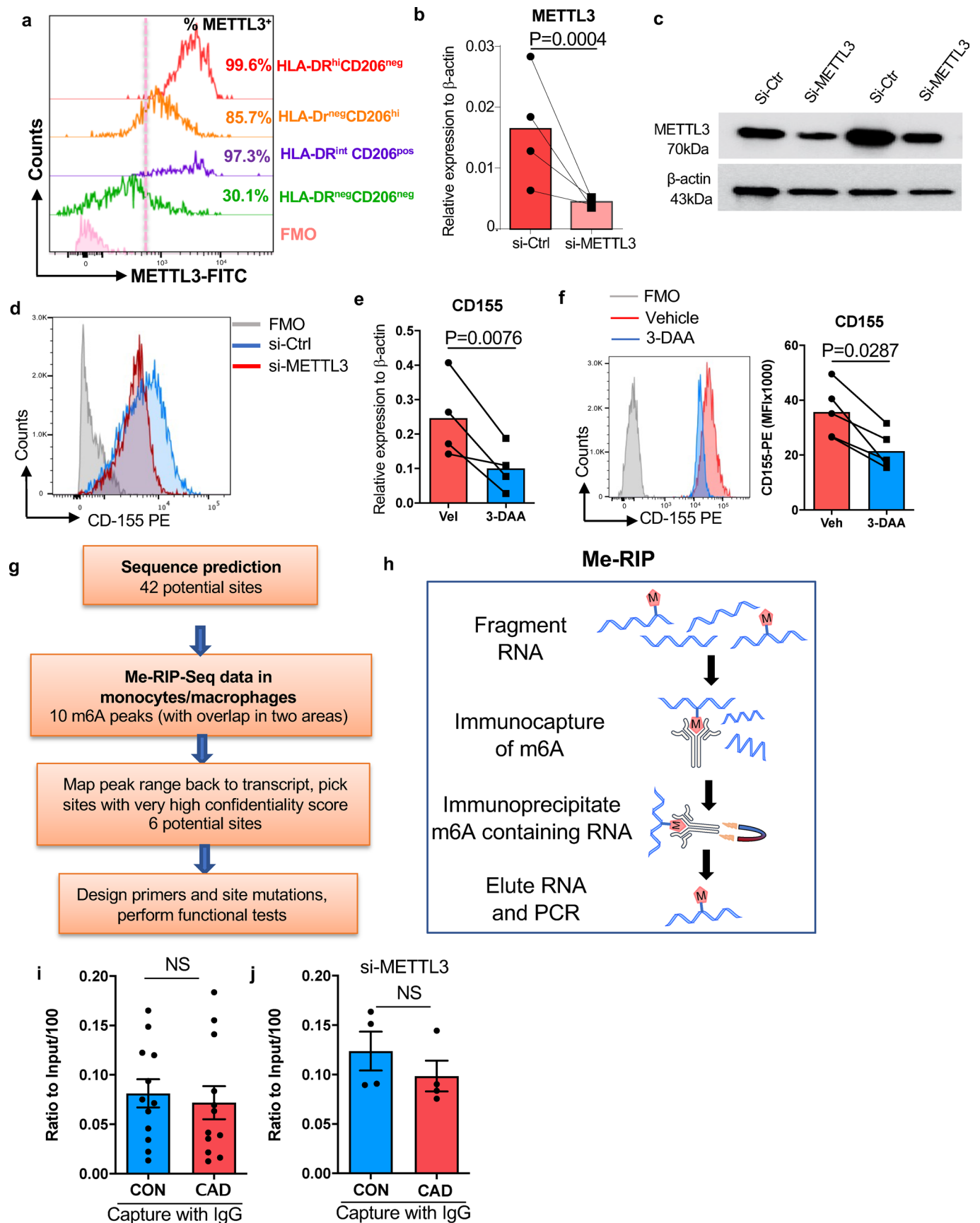
**Extended Data Fig. 3 | CD155 expression in tissue macrophages and in monocyte-derived macrophages.** a. Single cell suspensions were generated from human atherosclerotic arteries and analyzed by flow cytometry. Gating strategy to identify CD68<sup>+</sup> macrophages. Corresponded to panel b, c, and Extended data Fig. 6. b. Representative plot graphs from 2 tissues defining co-expression of CD206 and HLA-DR. c. Surface expression of CD155 on different tissue macrophage clusters. Data from two tissues are shown. d. Monocyte-derived macrophages (M $\phi$ ) were treated with either LPS (100 ng/ml)+ IFN-g(100 u/ml) or IL-4 (20 ng/ml). Surface CD155 expression was determined by FACS. Representative histograms and mean  $\pm$  SEM of mean fluorescence intensities from 6 experiments. Two-tailed student t test. P value shown on figure.



**Extended Data Fig. 4 | Efficiency of CD155 knockdown and impact of CD155 on anti-viral immune responses in healthy individuals.** a. Monocyte-derived macrophages (M $\phi$ ) were generated from patients and controls. Relative expression CD155 transcripts in healthy and CAD M $\phi$  (n=12). M $\phi$  were generated as in Fig. 2 and transfected with control or CD155 siRNA. b. CD155 transcripts were quantified by qPCR. c. CD155 expression on the surface of M $\phi$  detected by flow cytometry. n=8. T cells from healthy individuals were stimulated with viral antigen-loaded M $\phi$ . In parallel cultures, anti-CD155 antibodies were added or CD155 was knocked down by siRNA technology. Six hours later, antigen-responsive CD69 $^{+}$  CD40L $^{+}$  T cells were measured by flow cytometry. d. IFN- $\gamma$  secretion after SARS-CoV2 antigen stimulation in the absence and presence of anti-CD155 antibodies. n=10 each. e. IFN- $\gamma$  secretion after EBV antigen stimulation in the absence and presence of anti-CD155 antibodies. n=5 each. f. Frequencies of anti-SARS-CoV2 CD69 $^{+}$  CD40L $^{+}$  T cells after CD155 blockade. n=8. g. Frequencies of anti-EBV CD69 $^{+}$  CD40L $^{+}$  T cells after CD155 blockade. n=5. h. IFN- $\gamma$  release induced by SARS-CoV2 antigen-pulsed CD155 siRNA-transfected M $\phi$ . n=10. i. IFN- $\gamma$  release induced by EBV antigen-pulsed CD155 siRNA-transfected M $\phi$ . n=5. j. Frequencies of anti-SARS-CoV2 CD69 $^{+}$  CD40L $^{+}$  T cells after CD155 knockdown. n=8. k. Frequencies of anti-SARS-CoV2 CD69 $^{+}$  CD40L $^{+}$  T cells after CD155 knockdown. n=5. Individual data points are displayed. Data are mean  $\pm$  SEM. Differences were compared with 2 tail student t test. p-value was shown on each panel.

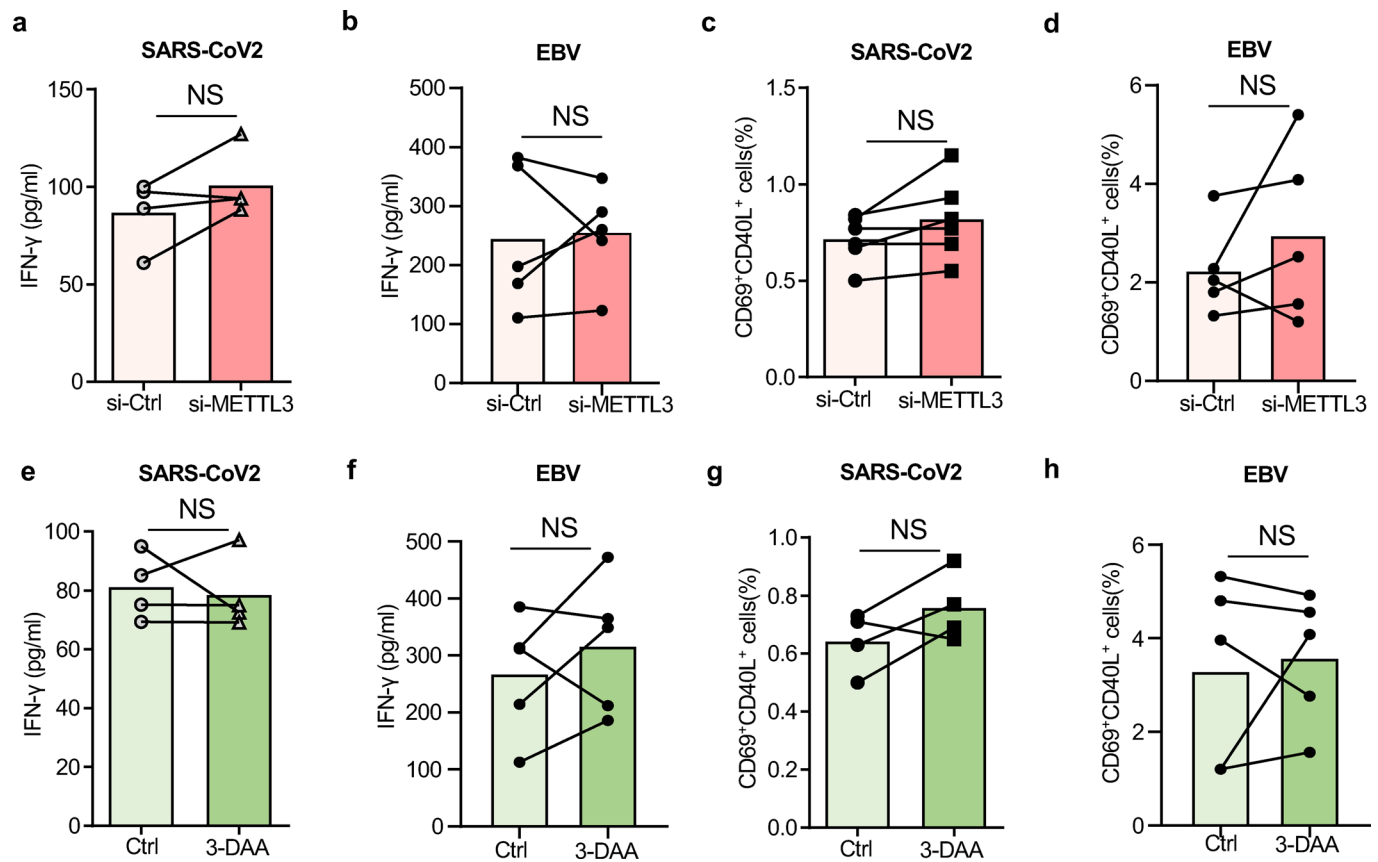


**Extended Data Fig. 5 | Macrophage survival.** a.-d. Monocytes were isolated and differentiated into macrophages (M $\phi$ ) with M-CSF over 5 days. Cell survival rates were quantified by 3 different approaches: a.-b. Simultaneous Live/dead cell staining with calcein AM (live) and BOBO-3 (dead). (a) Representative image from 3 independent experiments. (e) Cell survival rates from 12 controls and 12 patients. c. Cell death was measured by LDH release. Data from 12 controls and 12 patients. d. Cell viability was measured by staining with the alamarBlue cell viability reagent. Data from 12 controls and 12 patients. e.-h. Monocyte-derived macrophages (M $\phi$ ) were transfected with control siRNA, CD155-specific si-RNA or METTL3-specific siRNA. Cell survival was quantified after 48 hrs. (e) Calcein AM (live) / BOBO-3 (dead) staining. Representative images from 8 experiments in each group. (f) Cell death rates measured in all 8 experiments. (g) LDH release measured in all 8 experiments. (h) AlamarBlue cell viability staining. Data from 8 experiments. Individual data points are displayed. Data are mean  $\pm$  SEM. Differences were compared with one-way ANOVA.

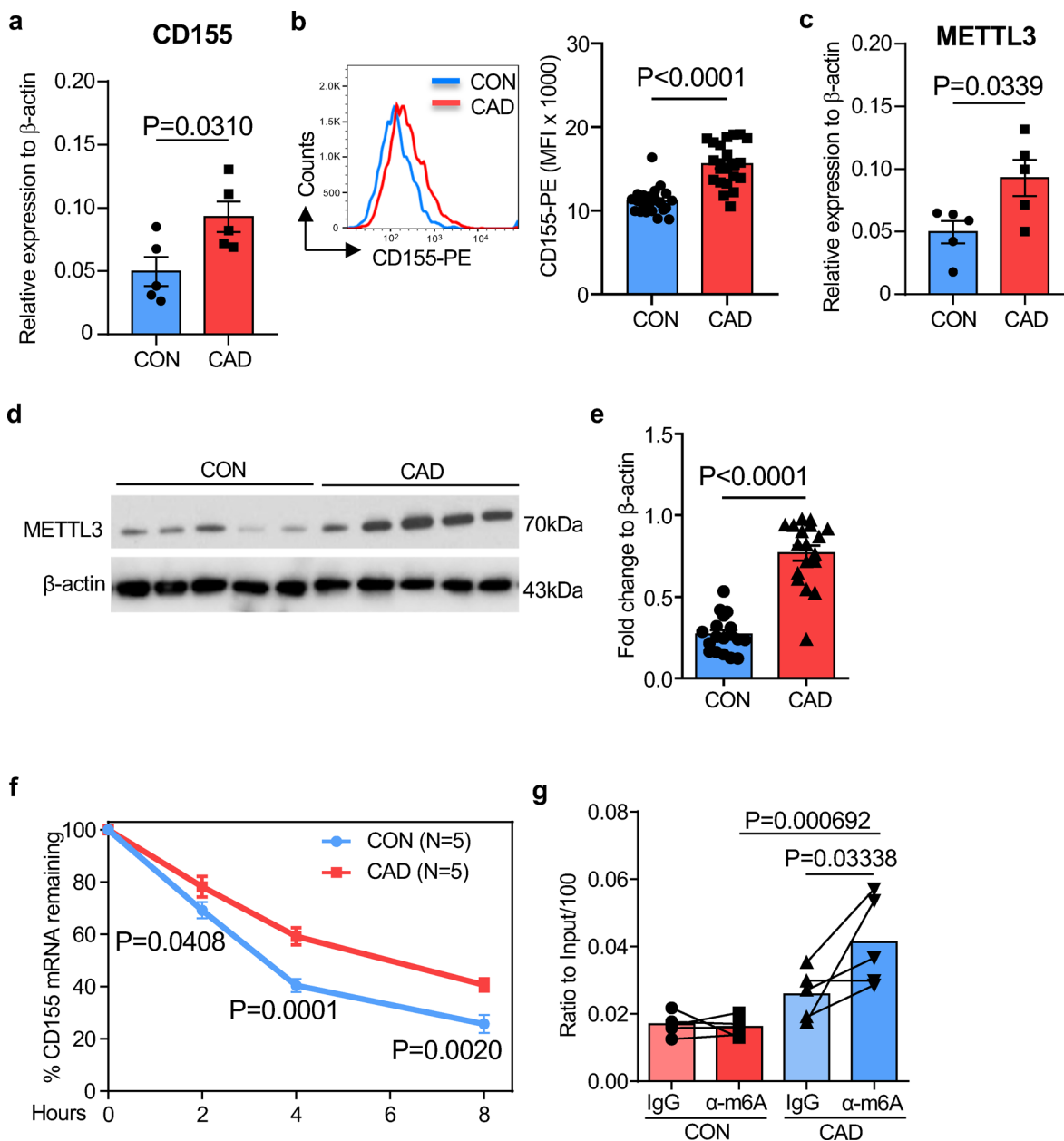


Extended Data Fig. 6 | See next page for caption.

**Extended Data Fig. 6 | Tissue METTL3, efficiency of METTL3 knockdown, strategy of predicting methylation sites and Me-RIP quantification.** a. Human atherosclerotic arteries were collected and analyzed by flow cytometry as Extended Data Figs. 3a-b shown. Intranuclear expression of METTL3 on different tissue macrophage clusters. M $\phi$  were generated from monocyte precursors of healthy individuals and CAD patients as in Fig. 1. b. Knockdown efficiency for METTL3 in control and patient-derived M $\phi$ . Cells were transfected with METTL3 siRNA and METTL3 transcripts were quantified by RT-PCR (n = 4 experiments). c. METTL3 protein expression was determined by Western blotting (n = 2 control-CAD pairs). d. Representative histogram for CD155 expression on macrophages after knockdown of METTL3. e.-f. M $\phi$  were treated with the m6A inhibitor 3-DAA. (e) CD155 transcripts were quantified by RT-PCR. N = 4. (f) CD155 protein expression was measured by FACS. Representative histogram (left) and mean fluorescence intensity (right) from 5 experiments. g. Scheme delineating the process of determining m6A sites on CD155 mRNA. h. Scheme depicting the method to quantify Me-RIP. i.-j. Immunoprecipitation of Methylated RNA (Me-RIP) with IgG control antibody. i. CD155 mRNA was precipitated with IgG control antibody in healthy and CAD M $\phi$  and quantified by Me-RIP. N = 12 experiments. j. METTL3 was knocked down in control and CAD M $\phi$  by siRNA technology. CD155 mRNA was precipitated with IgG antibody and measured by Me-RIP. N = 4 experiments. Individual data points are displayed. Data are mean  $\pm$  SEM. Differences were compared with two tail student t test. p-value was shown on each panel.



**Extended Data Fig. 7 | Viral antigen presentation after inhibition of m6A modification in healthy M $\phi$ .** a.-d. M $\phi$  generated from healthy individuals were transfected with METTL3 siRNA and subsequently used as antigen-presenting cells to stimulate anti-viral T cells. a. IFN- $\gamma$  release in response to SARS-CoV2 antigen quantified in 4 experiments. b. IFN- $\gamma$  release in response to EBV antigen quantified in 5 experiments. c. Frequencies of SARS-CoV2 specific CD69 + CD40L + CD4 + T cells measured in 6 experiments. d. Frequencies of EBV specific CD69 + CD40L + CD4 + T cells measured in 5 experiments. e.-h. M $\phi$  from healthy individuals were treated with the m6A inhibitor 3-Deazaadenosine (3-DAA), loaded with antigen and mixed with T cells. e. IFN- $\gamma$  release in response to SARS-CoV2 antigen quantified in 4 experiments. f. IFN- $\gamma$  release in response to EBV antigen quantified in 5 experiments. g. Frequencies of SARS-CoV2 specific CD69 + CD40L + CD4 + T cells measured in 6 experiments. h. Frequencies of EBV specific CD69 + CD40L + CD4 + T cells measured in 5 experiments. Individual data points are displayed. Data are mean  $\pm$  SEM. Differences were compared with one-way ANOVA.



**Extended Data Fig. 8 | CD155hi METTL3hi monocytes in patients with CAD.** CD14<sup>+</sup> monocytes were isolated from the blood of CAD patients and age-matched controls. a. CD155 transcripts quantified by RT-PCR. b. Flow cytometry for CD155 protein expression. Representative histogram and data from 5 experiments. c. METTL3 transcripts measured by RT-PCR (n=5). d.-e. Quantification of METTL3 protein by immunoblot in monocytes from 5 patients and 5 controls.  $\beta$ -actin served as loading control. f. CD155 mRNA decay assay in control and CAD monocytes (n=5). g. Methylated CD155 mRNA measured by Me-RIP in control and CAD monocytes (n=5). Individual data points are displayed. Data are mean  $\pm$  SEM. Differences were compared with one-way ANOVA. p-value was shown on each panel.

Extended Data Table 1 | Clinical characteristics of patients with CAD

Parameters	N=87
Age (mean $\pm$ SD)	68.51 $\pm$ 8.40
Male	78.16%
<b>Ethnicity</b>	
Caucasian	66.7%
African-American	11.2%
Asian	13.8%
Hispanic	8.0%
BMI (mean $\pm$ SD)	29.81 $\pm$ 6.70
Diabetes mellitus	24.1%
Hypertension	58.6%
Hyperlipidemia	55.2%
Family history of CAD	27.6%
EBV exposure	83.9%
<b>Smoking</b>	
Current	4.6%
Former	44.8%
<b>Coronary Artery Disease</b>	
Myocardial ischemia	25.3%
Coronary artery bypass grafting	29.9%
Percutaneous Coronary Intervention	64.3%
<b>Treatment</b>	
ACE inhibitor	39.1%
ATII receptor blocker	24.1%
$\beta$ -blocker	71.3%
Ca-antagonist	20.7%
Diuretic	13.8%
Anti-platelet	68.9%
Anti-coagulant	43.7%
Statin	78.1%
Biguanide	13.8%
Insulin	10.3%

**Extended Data Table 2 | Lipid profiles for plasma donors**

	TG <sup>hi</sup> (n=4)	TG <sup>lo</sup> LDL <sup>hi</sup> (n=7)	TG <sup>lo</sup> LDL <sup>lo</sup> (n=4)
Total cholesterol (mg/dl)	173.75±13.86	236.33±23.29	185.5±23.76
HDL (mg/dl)	40.25±9.73	70±20.93	77.25±24.98
LDL (mg/dl)	91.5±8.73	148.5±29.08	93.5±9.34
Triglyceride (mg/dl)	208.75±34.83	90±19	74.25±14.94
Non-HDL-C (mg/dl)	133.5±5.39	166.33±31.25	100±22.17

## Reporting Summary

Nature Portfolio wishes to improve the reproducibility of the work that we publish. This form provides structure for consistency and transparency in reporting. For further information on Nature Portfolio policies, see our [Editorial Policies](#) and the [Editorial Policy Checklist](#).

### Statistics

For all statistical analyses, confirm that the following items are present in the figure legend, table legend, main text, or Methods section.

- |     |           |
|-----|-----------|
| n/a | Confirmed |
|-----|-----------|
- The exact sample size ( $n$ ) for each experimental group/condition, given as a discrete number and unit of measurement
  - A statement on whether measurements were taken from distinct samples or whether the same sample was measured repeatedly
  - The statistical test(s) used AND whether they are one- or two-sided  
*Only common tests should be described solely by name; describe more complex techniques in the Methods section.*
  - A description of all covariates tested
  - A description of any assumptions or corrections, such as tests of normality and adjustment for multiple comparisons
  - A full description of the statistical parameters including central tendency (e.g. means) or other basic estimates (e.g. regression coefficient) AND variation (e.g. standard deviation) or associated estimates of uncertainty (e.g. confidence intervals)
  - For null hypothesis testing, the test statistic (e.g.  $F$ ,  $t$ ,  $r$ ) with confidence intervals, effect sizes, degrees of freedom and  $P$  value noted  
*Give  $P$  values as exact values whenever suitable.*
  - For Bayesian analysis, information on the choice of priors and Markov chain Monte Carlo settings
  - For hierarchical and complex designs, identification of the appropriate level for tests and full reporting of outcomes
  - Estimates of effect sizes (e.g. Cohen's  $d$ , Pearson's  $r$ ), indicating how they were calculated

*Our web collection on [statistics for biologists](#) contains articles on many of the points above.*

### Software and code

Policy information about [availability of computer code](#)

Data collection

Data analysis

For manuscripts utilizing custom algorithms or software that are central to the research but not yet described in published literature, software must be made available to editors and reviewers. We strongly encourage code deposition in a community repository (e.g. GitHub). See the Nature Portfolio [guidelines for submitting code & software](#) for further information.

### Data

Policy information about [availability of data](#)

All manuscripts must include a [data availability statement](#). This statement should provide the following information, where applicable:

- Accession codes, unique identifiers, or web links for publicly available datasets
- A description of any restrictions on data availability
- For clinical datasets or third party data, please ensure that the statement adheres to our [policy](#)

All data that support the findings of this study are available from the corresponding author upon reasonable request. For m6A peak analysis, datasets GSE76414 and GSE87190 from NCBI GEO database browser were used. The matrix file for both datasets were published on GEO website with free access. No further code was applied to data analysis.

## Field-specific reporting

Please select the one below that is the best fit for your research. If you are not sure, read the appropriate sections before making your selection.

Life sciences  Behavioural & social sciences  Ecological, evolutionary & environmental sciences

For a reference copy of the document with all sections, see [nature.com/documents/nr-reporting-summary-flat.pdf](https://www.nature.com/documents/nr-reporting-summary-flat.pdf)

## Life sciences study design

All studies must disclose on these points even when the disclosure is negative.

Sample size	No sample size calculation was performed. At least 3 independent were performed for each panel. Sample size to identify differences between patients and controls or between patient subsets were chosen to ensure 80% power with a level of significance of 5% when the difference in their means would be 1.5 standard deviation ( $n \geq 10$ ). To assess the effect of in vitro intervention (e.g. gene silencing, metabolite exposure), we used paired testing with a sample size of 3 to 5. For in vivo experiments, 5 mice were enrolled in each treatment arm.
Data exclusions	No data was excluded.
Replication	All data are repeat for at least 3 times. All attempts at replication were successful. All data were included in the paper.
Randomization	PBMCs from control and patient donors were assigned randomly in each experiment. To implement random assignment, assign a unique number to every member of our study's sample. Then, we use a random number generator to randomly assign each number to a control or experimental group. For in vivo study, mice were randomly assigned to different study groups.
Blinding	Blinding analysis was applied to all data. The investigators were blinded to group allocation during data collection.

## Reporting for specific materials, systems and methods

We require information from authors about some types of materials, experimental systems and methods used in many studies. Here, indicate whether each material, system or method listed is relevant to your study. If you are not sure if a list item applies to your research, read the appropriate section before selecting a response.

### Materials & experimental systems

n/a	Involved in the study
<input type="checkbox"/>	<input checked="" type="checkbox"/> Antibodies
<input checked="" type="checkbox"/>	<input type="checkbox"/> Eukaryotic cell lines
<input checked="" type="checkbox"/>	<input type="checkbox"/> Palaeontology and archaeology
<input type="checkbox"/>	<input checked="" type="checkbox"/> Animals and other organisms
<input type="checkbox"/>	<input checked="" type="checkbox"/> Human research participants
<input checked="" type="checkbox"/>	<input type="checkbox"/> Clinical data
<input checked="" type="checkbox"/>	<input type="checkbox"/> Dual use research of concern

### Methods

n/a	Involved in the study
<input checked="" type="checkbox"/>	<input type="checkbox"/> ChIP-seq
<input type="checkbox"/>	<input checked="" type="checkbox"/> Flow cytometry
<input checked="" type="checkbox"/>	<input type="checkbox"/> MRI-based neuroimaging

## Antibodies

Antibodies used

Brilliant Violet 785™ anti-human CD154 BioLegend Cat#310842,RRID:AB\_2572187,Clone:24-31,Flow:1:100  
 Brilliant Violet 510™ anti-human CD69 Antibody BioLegend Cat#310936,RRID:AB\_2563834,Clone:FN50,Flow:1:100  
 Brilliant Violet 421™ anti-human CD3 Antibody BioLegend Cat#344834,RRID:AB\_2565675,Clone:SK7,Flow:1:100  
 PE/Cyanine7 anti-human CD4 Antibody BioLegend Cat#357410,RRID:AB\_2565662,Clone:A161A1,Flow:1:100  
 Brilliant Violet 650™ anti-human CD8 Antibody BioLegend Cat#344730,RRID:AB\_2564510,Clone:SK1,Flow:1:100  
 APC/Cyanine7 anti-human CD45RA Antibody BioLegend Cat#304128,RRID:AB\_10708880,Clone:HI100,Flow:1:100  
 FITC anti-human CD45RO Antibody BioLegend Cat#304242,RRID:AB\_2564159,Clone:UCHL1,Flow:1:100  
 PerCP/Cyanine5.5 anti-human CD38 Antibody BioLegend Cat#356614,RRID:AB\_2562183,Clone:HB-7, Flow:1:100  
 Brilliant Violet 711™ anti-human CD163 Antibody BioLegend Cat#333630,RRID:AB\_2650972,Clone:GHI/61,Flow:1:100  
 PE/Cyanine7 anti-human CD45 Antibody BioLegend Cat#368532,RRID:AB\_2715892,Clone:2D1,Flow:1:100  
 Brilliant Violet 711™ anti-human CD4 Antibody BioLegend Cat#317439,RRID:AB\_11219404,Clone:OKT4,Flow:1:100  
 Pacific Blue™ anti-human HLA-DR Antibody BioLegend Cat#307624, RRID:AB\_493665,Clone:L243,Flow:1:100  
 APC anti-human CD206 (MMR) Antibody BioLegend Cat#321110, RRID:AB\_571885,Clone:15-2,Flow:1:100  
 PE anti-human CD155 (PVR) BioLegend Cat# 337610, RRID:AB\_2174019,Clone:SKII.4,Flow:1:100  
 Goat anti-Rabbit IgG (H+L) Secondary Antibody, FITC,Thermo Fisher Scientific,Cat#A-31635, RRID:AB\_429708,Polyclonal,Flow:1:100  
 Biotin Anti-Human CD154 BioLegend Cat#317439,RRID:AB\_492966,Clone:OKT4,Flow:1:100  
 CD40 Monoclonal Antibody (5C3), eBioscience™ Thermo Fisher Scientific Cat#14-0409-82,RRID:AB\_467232,Clone:5C3, signal block:1µg/ml  
 CD155 Monoclonal Antibody (D171) Thermo Fisher Scientific Cat#MA5-13493, RRID:AB\_10978147,Clone:D171,IF:1:200

CD68 Monoclonal Antibody (KP1) Thermo Fisher Scientific Cat#MA5-13324, RRID:AB\_10987212, Clone:KP1, IF:1:200  
 CD96 Polyclonal Antibody Thermo Fisher Scientific Cat#PA5-97568, RRID:AB\_2812183, Flow:1:100  
 TIGIT (E5Y1W) XP® Rabbit mAb Cell Signaling Technology Cat#99567S, Clone:E5Y1W, Flow: 1:100  
 METTL3 (E3F2A) Rabbit mAb Cell Signaling Technology Cat#86132S, RRID:AB\_2800072, Clone:E3F2A, western blot:1:500, Flow:1:80  
 Goat anti-rabbit IgG (H+L), Alexa Fluor 488 Thermo Fisher Scientific Cat#A-11008, RRID:AB\_143165, Polyclonal, IF:1:200  
 Goat anti-mouse IgG (H+L), Alexa Fluor 594 Thermo Fisher Scientific Cat#A-11032, RRID:AB\_2534091, Polyclonal, IF:1:200  
 Mouse monoclonal anti-b-Actin Cell Signaling Technology Cat#3700S, RRID:AB\_2242334, Clone:8H10D10, Western Blot:1:500

Validation

All antibodies used in this study are commercialized and have been validated by the manufacture. The validation statements are available on the manufacturer's website

## Animals and other organisms

Policy information about [studies involving animals](#); [ARRIVE guidelines](#) recommended for reporting animal research

Laboratory animals

"NOD.Cg-Prkdcscidll2rgtm1Wjl/SzJ (NSG) mice were obtained from Jackson lab and bred in Mayo animal facility under specific pathogen-free conditions on a 12/12 h light/ dark cycle at 20-22°C, 40-60% humidity with free access to water and food. Both male and female mice from 8-12 weeks were used. Same sex of mice were used in each parallel experiment.

Wild animals

This study doesn't involve wild animal.

Field-collected samples

This study doesn't involve sample collected from field.

Ethics oversight

The animal study ethics were overseen by Administrative Panel on Laboratory Animal Care (APLAC), Stanford University and Mayo Clinic Institutional Animal Care and Use Committee. All experiments were approved and performed in accordance with the guidelines of the Institutional Animal Care and Use Committee.

Note that full information on the approval of the study protocol must also be provided in the manuscript.

## Human research participants

Policy information about [studies involving human research participants](#)

Population characteristics

Patients were defined to have coronary artery disease if they had a history of coronary bypass surgery, history of coronary stent placement or documented myocardial infarction. To eliminate inflammatory activity directly related to myocardial ischemia, 87 patients were enrolled that were at least 90 days post event. The average age of CAD patients are  $68.51 \pm 8.40$  years, age-matched controls were used in this study. 78% participants were male. Detailed clinical features of enrolled patients are displayed in Supplement Table 1. Healthy controls had no evidence for coronary artery disease as based on evaluation by a physician.

Recruitment

Patients were defined to have coronary artery disease if they had a history of coronary bypass surgery, history of coronary stent placement or documented myocardial infarction. To eliminate inflammatory activity directly related to myocardial ischemia, 87 patients were enrolled that were at least 90 days post event. Detailed clinical features of enrolled patients are displayed in Supplement Table 1. Healthy controls had no evidence for coronary artery disease as based on evaluation by a physician. Recruitment criteria included: no personal history of cancer, chemotherapy, chronic inflammatory disease, chronic viral infection, or autoimmune disease. No potential self-selection bias or other biases in recruitment.

Ethics oversight

The Institutional Review Board of Stanford University and Mayo Clinic reviewed and approved the study protocol. All participants were informed appropriately, written consent documents were signed by all participants.

Note that full information on the approval of the study protocol must also be provided in the manuscript.

## Flow Cytometry

### Plots

Confirm that:

- The axis labels state the marker and fluorochrome used (e.g. CD4-FITC).
- The axis scales are clearly visible. Include numbers along axes only for bottom left plot of group (a 'group' is an analysis of identical markers).
- All plots are contour plots with outliers or pseudocolor plots.
- A numerical value for number of cells or percentage (with statistics) is provided.

### Methodology

Sample preparation

Peripheral blood mononuclear cells (PBMC) were purified by density gradient centrifugation with Lymphoprep (STEMCELL technologies) as previously describe. Memory CD4+ T cells were isolated by negative selection with Easysep human cell isolation kits (STEMCELL Technologies, #19157). Monocytes were isolated as previously reported. To induce macrophages, monocytes were treated with 20ng/ml of M-CSF (Biolegend) for 5 days in 10% FBS (Lonza) and were differentiated by

	stimulation with 100ng/ml LPS (Sigma Aldrich) and 100U/ml IFN- $\gamma$ (Sino Biologicals) for 24 hours.
Instrument	CYTEK NL-3000
Software	FlowJo v10.7.2 (Tree Star Inc)
Cell population abundance	The purity of cell population was consistently over 95% by flow cytometry.
Gating strategy	Fluorescence minus one (FMO) was used to separate the positive and negative populations for experiments.

Tick this box to confirm that a figure exemplifying the gating strategy is provided in the Supplementary Information.